Tectonic evolution of the Tianshan Akeyazi metamorphic complex (NW China)

Léa Bayet, Philippe Agard, Timm John, Martina Menneken, Zhou Tan, Jun Gao

Tectonic evolution of the Tianshan Akeyazi metamorphic complex (NW China)

Léa Bayet[1,2], Philippe Agard[2], Timm John[1], Martina Menneken[1, 3], Zhou Tan[4] and Jun Gao[4]

[1]*Institut für Geologische Wissenschaften, Freie Universität Berlin, Malteserstr. 74–100, 12449 Berlin, Germany*

[2]*ISTEP, UMR CNRS 7193, Sorbonne Université, F-75005 Paris, France*

[3]*Institut für Geowissenschaften, Universität Bonn, Meckenheimer Allee 171, 53115 Bonn, Germany*

[4]*Institute of Geology and Geophysics, Chinese Academy of Sciences, P.O. Box 9825, Beijing 100029, China*

Abstract

The South Tianshan orogen (northwest China) comprises a thick volcanoclastic HP-UHP metamorphic belt, the Akeyazi (high-pressure) metamorphic complex (AMC), exhibiting well-preserved eclogite- and blueschist-facies rocks and pervasive deformation throughout all units. In order to clarify the tectonic evolution of this fossil subduction zone, which remains controversial due to the lack of systematic field observations combining structural and petrological data, we herein present the results of extensive mapping of lithologies, deformation patterns and petrological evolutions.

The AMC is composed of a high-pressure (HP) to ultra-high-pressure (UHP) central domain – the HP-UHP unit – separated in the North by a major detachment from a greenschist-facies domain. A gradational transition in lithologies (i.e., interlayered

micaschists, volcanoclastic, and mafic rocks) is observed within the HP-UHP unit, from more pelitic in the North to more mafic in the South. Tectonic patterns and contrasting lithologies allow to recognize five distinct sub-units stacked at HP to UHP conditions. Pervasive ductile deformation revealed by penetrative schistosities, folding, shear planes and boudinage structures is characterized by successive deformation stages which are attributed to burial (D_{n-1}), peak deformation accompanying detachment from the slab and/or deep nappe stacking (D_n, D_{n+1}) and exhumation (D_{n+2}, D_{n+3}). During exhumation under blueschist-facies conditions, the HP-UHP nappe stack underwent pervasive shearing, in particular across km-scale extensional shear zones with consistent top to the north shear senses reworking inherited thrust contacts. The entire HP-UHP unit reached peak-metamorphic conditions at ~2.5 GPa and ~540 °C. Peak pressures of 2.52 ± 0.25 GPa, consistent with the widespread occurrence of coesite in the HP-UHP unit, suggest a maximum burial depth of ~80 km which is thought to reflect a transition between mechanical coupling and decoupling at the plate interface. This tectono-metamorphic evolution is set back in a tentative geodynamic model.

1. Introduction

Over the past three decades numerous occurrences of ultra-high-pressure terranes have been reported worldwide (Chopin, 1984; Gillet et al., 1984; Kylander-clark et al., 2012; Liou et al., 2014, 2004; Smith, 1984), continuously questioning the mechanisms of burial and exhumation (e.g., Agard et al., 2009, 2018; Chopin, 2003; Guillot et al., 2009). By influencing viscosity and density, and thus buoyancy, the diversity of subducted material can lead to contrasting mechanical and chemical behaviors along the plate interface (Bebout, 2007; Bebout et al., 2013; Yamato et al., 2007; Behr and Becker, 2018).

Subducted material derived from the lower plate consists of the uppermost part of the subducting oceanic slab, i.e. pelagic sediments with basaltic oceanic crust and/or seamounts

(e.g., Ranero et al., 2008). Additional contribution from the upper plate may consist of ashes from arc-volcanism (e.g., Kutterolf et al., 2008b), pelagic and detrital sediments located in the accretionary prism or in the trench, and/or basement or mantle wedge material if basal erosion occurs (Polino, 1990; Roda et al., 2012; Scholl et al., 1980). Whether subduction is primarily in accretion or erosion mode thus partly controls what kind of material is supplied to the plate interface (Clift and Vannucchi, 2004; Cloos and Shreve, 1988a, 1988b) and partly returned in exhumed high-pressure ophiolite sequences (e.g., Angiboust et al., 2009; John et al., 2010; Luoni et al., 2018).

Whatever their respective contributions, materials from the lower and upper plate will be transported on top of the downgoing plate into subduction and may be stripped from the slab as tectonic slices (e.g., Angiboust and Agard, 2010; Laurent et al., 2016; Roda et al., 2012), mélanges (Festa et al., 2012; Grigull et al., 2012; Lázaro et al., 2009) and/or possibly get mixed via deformation and fluid-rock interaction processes (e.g., Bebout and Penniston-Dorland, 2016; Marschall and Schumacher, 2012). Burial and exhumation at the plate interface are accompanied by intense deformation, so that the plate interface is regarded by many as a large-scale shear zone (e.g., Cloos and Shreve, 1996; Raimbourg et al., 2007; Rowe et al., 2013; von Huene et al., 2004; Wakabayashi, 2015; Agard et al., 2018).

To unravel the fate of subducted material during burial and further constrain exhumation processes, we herein present a tectono-metamorphic study of the the Akeyazi (high-pressure) metamorphic complex (AMC, northwestern China), which is characterized by an unusually ca. 4-5 km thick pile of well-preserved high- to ultra-high-pressure (HP-UHP) metasedimentary and metavolcanoclastic rocks with numerous coesite findings (Bayet et al., 2018; Chen et al., 2011; Li et al., 2012; Lü et al., 2009; Lü and Zhang, 2012; Tian and Wei, 2013). Former studies focused on individual pressure-temperature-time paths (e.g., Tan et al., 2017 and references therein; Fig. 1a) and on detailed geochemical and petrological

investigations (Beinlich et al., 2010; Gao et al., 1995; Gao and Klemd, 2001; John et al., 2012; Klemd et al., 2002; Li et al., 2016; Lü et al., 2009; van der Straaten et al., 2008; Wei et al., 2003). In contrast, the regional structures and tectonic evolution remain poorly studied, except from local studies in the Kebuerte and Atantayi valleys (Soldner et al., 2017; Tan et al., 2017, 2019, Fig 2c). The lack of systematic petrostructural data over the entire area, along with scattered P-T-t estimates, has led to two contradictory concepts for the structural evolution of the AMC. It is considered either as 1) a tectonic mélange, with rocks originating from various depths and subsequently juxtaposed during exhumation (e.g., Klemd et al., 2011, Fig. 1b), or as 2) consisting of two sub-units separated by a km-scale shear zone: a HP-UHP unit in the North (based on coesite findings) and a HP unit (coesite-free) in the South (e.g., Lü et al., 2012a, Fig. 1b).

We herein present a detailed study of the structural and lithological relationships together with peak P-T estimates and propose a new geodynamic evolution for the AMC. Extensive mapping of tectonic boundaries, structures, deformation stages and systematic P-T determinations allow to place constraints on accretion mechanisms and the regional-scale tectono-metamorphic evolution.

2. Geological overview

The Tianshan orogenic belt was formed by the collision of the Tarim, Yili-Kazakh and Junggar plates during the Paleozoic (Gao et al., 2009; Han et al., 2011; Long et al., 2011; Xiao et al., 2009) and extends east-west over ~2500 km in central Asia. This orogen is part of the southwestern Central Asian Orogenic Belt (CAOB) (e.g., Jahn et al., 2000; Fig. 2a). The CAOB is referred to as a “tectonic collage” of several subduction zones. In the southwestern Tianshan, the suture between the Yili-Tianshan and Tarim plates exposes a metamorphic belt over ~1500 km from NW China to Tajikistan (Gao et al., 1998, 1995; Hegner et al., 2010; Volkova and Budanov, 1999; Fig. 2b). The subduction polarity

98 associated with this metamorphic belt is still debated, with some studies suggesting a
99 northward polarity, i.e. underneath the Yili plate (e.g., Charvet et al., 2011; Wang et al.,
100 2011), while others argue for a southward polarity, i.e. underneath the Tarim plate (e.g., Gao
101 et al., 1998, 1995; Soldner et al., 2017; Xiao and Santosh, 2014).

102 The area studied here is located in northwestern China and is part of this metamorphic
103 belt. It is bordered by two main structures: the south Central Tianshan Suture (SCTS) in the
104 North and the Northern Haerkeshan Peak Fault in the South (Fig. 2c; Gao et al., 1999; van
105 der Straaten et al., 2008). After being activated as a thrust contact, the SCTS was reactivated
106 with a dextral strike slip movement (Gao et al., 1995). It separates the AMC from volcanic
107 and volcanoclastic rocks belonging to the Yili-Tianshan plate in the North. The Northern
108 Haerkeshan Peak Fault defines the boundary between the metamorphic belt and the marbles
109 of the Tarim plate in the South.

110 The AMC (Klemd et al., 2015; Li et al., 2016; Meyer et al., 2016) consists of a high-
111 to ultra-high-pressure (HP-UHP)/low temperature unit in its center, and a greenschist-facies
112 unit separeted in two parts: one located in the North and another in the South (e.g., Gao and
113 Klemd, 2000; this study). The HP-UHP unit mainly consists of metavolcanoclastic and
114 metasedimentary rocks varying in composition (e.g., Gao and Klemd, 2003; this study). The
115 southernmost parts of the Akesayi and Atantayi valleys host a large body of eclogite to
116 blueschist-facies pillow basalts (Bayet et al., 2018; Gao et al., 1999), is correlated to the EB
117 unit of Tan et al. (2019). Available structural data is very limited at the scale of the studied
118 area (Gao et al., 1999). Only few schistosity measurements are reported, mostly in the
119 western part of the AMC, with a main ENE-WSW strike trend (Soldner et al., 2017; Tian
120 and Wei, 2013). Previous studies indeed focused mainly on single outcrops with detailed
121 reconstructions of pressure-temperature-time (P-T-t) paths, investigations of fluid-rock
122 interaction processes, or recovery of the geochemical budget in the HP-UHP unit (Beinlich

et al., 2010; Li et al., 2016; Lü et al., 2012b; Robinson et al., 1984; Tian and Wei, 2014; van der Straaten et al., 2008).

P-T metamorphic peak conditions in the studied area have been constrained using conventional geothermobarometry based on textural equilibrium, average P-T (using Thermocalc; Holland and Powell, 1998), and pseudosection modelling. The results of these studies provide very scattered estimates in the range of 330 to 650 °C at 1.4 to 3.2 GPa for peak metamorphic conditions, with the most accepted value at ~530 °C and ~2.1 GPa (e.g., Gao and Klemd, 2000; Klemd et al., 2011, 2005, Lü et al., 2012b, 2009, Wei et al., 2009, 2003).

Radiometric data on the dynamics of the belt span a wide range of ages. Peak burial of rocks now exposed in the AMC is estimated to have occurred between ~315 Ma and ~326 Ma with a main cluster at ~319 Ma, based on Lu-Hf and Sm-Nd dating of garnet and U-Pb zircon and rutile ages (e.g., Klemd et al., 2011; Liu et al., 2014; Soldner et al., 2017; Tan et al., 2017). Exhumation is less well constrained, with blueschist-facies to greenschist-facies conditions around ~310-305 Ma, based on Rb-Sr and Ar-Ar dating of white mica (Klemd et al., 2005).

3. Field observations: lithologies and structural data

Structural and lithostratigraphic data are shown in figures 3 to 6 through outcrop-scale observations of the different lithologies (Fig. 3), panoramic views of the Muzetekezie and Akesayi valleys (Fig. 5) and synthetic maps and cross-section (Figs. 4, 6). The link between lithologies, structures, metamorphism and deformation stages is summarized in Table 1.

The AMC can be divided into two major units: the high- to ultra-high-pressure (HP-UHP) unit in the south and a greenschist-facies (GS) unit in the North (Figs. 4a & 5a). The GS unit also crops out south of the AMC in the Kebuerte Valley (van der Straaten et al., 2008; Tan et al., 2019). The GS and HP-UHP units identified here are spatially correlated,

toward the west, with the GS1 and UH units of Tan et al. (2019), respectively. The GS and HP-UHP units are separated in the north by a large-scale tectonic contact extening from west to east for ~13 km, namely the greenschist/high-pressure detachment (GHPD; Figs. 5a). The GHPD is marked by a ~50-100 m thick zone of intense deformation (Fig. 5a). This contact was relocated slightly northward with respect to its former location based on our field observations (Fig. 6a). While the contact is conspicuous in the western and central parts it is more diffuse in the east, due to the tectonic imbrication of greenschists with higher grade metamorphic rocks close to the contact (Fig. 6a). In our study area the GS unit is mainly composed of metapelites containing chlorite-albite-actinolite ± white mica but lacking garnet (Fig. 3l). Schistosity measurements in the GS unit reveal a gentle synclinal fold in its central part vanishing towards the east. In the central part, the GS unit is unconformably overlain by unmetamorphosed micro-conglomerates and silts over a ~1 km^2 large area representing the remnants of a former sedimentary basin (Figs. 4a, 5a, 3m). We focus in the following on the HP-UHP unit.

3.1 Lithologies in the HP-UHP unit

The HP-UHP unit consists of a ~4-5 km-thick metavolcanoclastic sequence with great lithological variability: (i) 'pure' mica-rich metasediments (Fig. 3a), (ii) 'pure' mafic rocks (Fig 3c,d), both being often interlayered (Figs. 3f,g), (iii) layers of volcanoclastic rocks with intermediate composition (Fig. 3b,e), also interlayered with more pelitic (Fig 3 e, i, k) or mafic (Fig 3h, j) layers and (iv) carbonates and marbles present as veins (cm-dm), layers and bodies intercalated with volcanoclastic rocks (Fig. 3n).

To evaluate lithological variations within the HP-UHP unit, we classified lithologies according to the proportion of volcanic and sedimentary components, ranging from a 'purely' mafic metavolcanic rock (hereafter referred to as M-type) to a 'pure' micaschist (S-type), with intermediate metavolcanoclastic compositions (V-type). V-type rocks generally

contain a high proportion of white mica and lesser amounts of amphibole and/or clinopyroxene compared to purely mafic rocks.

Micaschists dominate in the North, with a small proportion of mafic components and mafic rocks, only present as thin layers or small boudins (Fig. 4b; topmost part of section). Across the study area, the lithology varies gradually from more pelitic in the North to more mafic in the South (Figs. 4a,b). The mafic component increases southward through the presence of large-scale lenses and m- to km-thick continuous mafic horizons, which can be mapped for up to a few kilometers. The southernmost accessible part of the HP-UHP unit consists of a large body, trending E-W over 3-4 km, of pillow basalts (Fig. 3p), and pillow breccias interlayered with radiolarian cherts (Fig. 3q). Due to the presence of glaciers and very difficult access further south, its southern extension remains ill-constrained.

Rocks in the HP-UHP unit underwent blueschist- to eclogite-facies metamorphism, as indicated by the occurrence of index HP and UHP minerals (e.g., omphacite, glaucophane, garnet, coesite), the presence of formerly lawsonite-bearing blueschist (Fig. 3d), glaucophanite (Fig. 3o) and eclogite s.s. (Fig. 3c). An occasional greenschist-facies overprint can be found in the HP-UHP unit.

3.2 Tectonic overview and sub-units within the HP-UHP unit

The HP-UHP unit experienced intense deformation marked by penetrative schistosities, folding, boudinage and stretching lineations (Figs. 5 to 8). Schistosity, folding and shearing tend to localize in the more pelitic lithologies, while the mafic lithologies are less affected by deformation (Fig. 3). At the km-scale, the attitude of the main schistosity (hereafter termed S_n) appears relatively monotonous (Figs. 5b,c, 6a), with an average schistosity pole value around N085 30N (Fig. 6b). This apparent continuity is interrupted by several km-scale, mappable shear zones with systematical top to the north shear senses, and thus normal kinematic (Fig. 6a, c), which locally deflect the main schistosity and some

large-scale markers such as carbonate horizons. These large-scale shear zones are meter to several meter wide, highly deformed zones outlined by an increase in the density of shear bands and/or overprinting crenulation. Ductile shearing is marked at all scales by S/C fabrics and fish structures (e.g. Figs. 3k, 6e). C' planes strike ~N060 on average throughout the area (Fig. 6c), with consistent top-to-the-north shear senses, and thus apparent normal kinematics (Figs. 6e). C' planes commonly evidence recrystallization of blue amphibole and dominantly N-S directed lineations (Fig. 6d). A synthetic cross-section for the area is shown in figure 6f. The large-scale shear zones, together with some changes in lithology (i.e., no marbles in sub-unit 4), allow to define five sub-units from north to south (Figs. 6a,f): sub-units 1 to 4 are characterized by metasedimentary to metamafic sequences while sub-unit 5, in the southernmost part of the study area, corresponds to a large, km-scale body of pillow basalts and associated radiolarian cherts.

3.3 Deformation stages and characteristic outcrop-scale deformation patterns

The main schistosity shown in figures 6e,f is in fact composite in many places, particularly near mafic boudins or shear zones: it is made of a dominant schistosity variably overprinted by crenulation, in places so pervasive that both cannot be distinguished. These planar structures are termed Sn and Sn+1, respectively. Ductile shear bands and C' planes cross-cutting them are therefore referred to as Dn+2 (Fig. 6e). For the sake of clarity, figure 6g features the various deformation stages found across the study area and their cross-cutting relations. Table 1 provides a more detailed account of the systematic characteristics allowing to define successive deformation patterns.

Boudinage, crenulation schistosity and C’ structures reworking the main schistosity, and minerals associated with these successive deformation steps, are best observed in the HP-UHP unit at the outcrop scale and/or in thin-section. Figures 7a,b show the shear zone

223 separating units 1 and 2, which consists of a ~1 m thick mylonitic shear band with S/C
224 structures in metapelitic rocks and boudinaged mafic rocks. Figures 7c,d show a typical
225 boudin wrapped into a more pelitic lithology and features characteristic of successive
226 deformation events.

227 The crenulation schistosity (S_C) is observed across the entire area (e.g., Fig. 7d). As
228 for S_n, S_C strikes ENE-WSW but with a higher dip angle. It fully overprints S_n in strongly
229 deformed areas or along shear bands so that the main schistosity there is in fact S_{n+1} (e.g.,
230 Figs. 7e,f). Tight and recumbent folding visible at the cm- to km-scale, commonly with axial
231 planes parallel to S_{n+1}, is therefore mostly associated to the Dn+1 deformation stage (e.g.,
232 Fig. 7h; Table 1). Large-scale folds, most obvious for metacarbonate horizons, strike N080
233 on average (Fig. 6a). Most of these recumbent folds rework peak burial eclogite-facies
234 parageneses (see § Petrology below), suggesting that Dn+1 occurs at least partly during (the
235 start of) exhumation. Some cm-scale sheath folds accompanied by blue amphibole
236 overgrowths may correspond to Dn+1 and/or Dn+2 (Fig. 7i).

237 Figure 7g,j show C and C' planes of Dn+2 stage reworking the Sn+n+1 composite
238 schistosity with blue amphibole lineation. Some minor, less pervasive shear zones display
239 blue-green-amphibole (greenschist-facies) lineations with more randomly dispersed
240 directions (Fig. 6d). They commonly occur as cm- to meter-scale brittle to ductile, high-
241 angle C' structures, oblique to C_{n+2} planes (Fig. 7k, l), and are dominantly associated with
242 chlorite overgrowths. These greenschist-facies shear zones cutting across or overprinting
243 blueschist-facies ones define a Dn+3 stage, possibly marking the transition from blueschist-
244 to greenschist-facies conditions (Table 1).

245

246 3.4 Deformation patterns at thin-section scale

Mafic rocks show little internal deformation, even at smaller scale (cm to mm), particularly when surrounded by metasediments: most minerals are euhedral and there is no foliation (Fig. 8a). Deformation intensifies together with an increasing white mica proportion in mafic rocks, both under eclogite- (Fig. 8b, c) and blueschist-facies conditions (Fig. 8d). Omphacite-bearing mafic rocks show much less deformation than amphibole-bearing mafic rocks.

At the hand specimen or thin-section scale, deformation is accommodated by the development of a schistosity (Dn to Dn+1) composed of white mica, quartz ± acicular amphibole. Pressure shadows develop around garnet (Figs. 8e,f). In the most deformed samples, quartz presents undulose extinction and dynamic recrystallization (Fig. 8e). In addition to deformation stages recognized in the field, a former deformation stage D_{n-1} can be identified in these garnets (Figs. 8g,h): quartz inclusions in garnet define an older schistosity, S_{n-1}, rotated as garnet grows and commonly at an angle with S_n (Fig. 8f). The crenulation schistosity (S_C, Fig.7e,f) develops in both V- and S-type rocks (Fig. 8g). Shearing associated with D_{n+2} is expressed as S/C structures, quartz pressure shadows around garnet, foliation fishes, boudinage and rotated garnets in shear bands (Fig. 8h).

4. Methodology: estimation of P-T conditions and analytical techniques

4.1 Estimation of peak pressure-temperature conditions

To assess metamorphic conditions of the area and reconstruct the tectono-metamorphic history, we estimated peak pressure-temperature conditions (P-T) of samples evenly distributed across the entire area using four different methods: 1) Raman spectroscopy on carbonaceous material (RSCM) thermometry, 2) Zr-in-rutile thermometry, 3) quartz-in-garnet (QuiG) barometry and 4) phengite (-garnet-omphacite) barometry.

The RSCM method (T_C) is based on the temperature dependent crystallinity of carbonaceous material, which irreversibly increases with increasing temperature. RSCM

thermometry thus allows to estimate peak temperatures and was calibrated over the 330-650 °C range (e.g., Beyssac et al., 2002). The Zr-in-rutile thermometry (T_{Zr}) is based on the Zr content in rutile and measured using the electron microprobe. With increasing temperature, rutile can incorporate more Zr into its structure, independently from the rock type (S, V or M). When quartz and zircon buffer the system the corresponding temperature can be calculated purely based on Zr-content in rutile (e.g., Zack et al., 2004). The Zr in rutile thermometer allows broad applications on various rock types over a large temperature range (430-1100 °C). We used the calibration of Ferry and Watson (2007). All measured rutiles have zircon in their close vicinity to buffer the Zr system. Inasmuch as possible, we avoided rutile with zircon exsolution or inclusions, which may bias the calculated temperatures (Meyer et al., 2011). We measured as many grains as possible from 10-15 µm up to a few centimeters to obtain better statistics and homogeneous results. Both thermometers are restricted by an absolute uncertainty of about ± 50 °C. Their precision, however, is estimated to be ± 10 °C, which reflects their high reproducibility (Beyssac et al., 2002; Zack et al., 2004).

Minimum peak pressures (P_Q) were estimated using quartz-in-garnet (QuiG) barometry following the method of Enami et al. (2007) and Ashley et al. (2014b). This method is based on the different elastic moduli of garnet and quartz, resulting in less compression of the garnet lattice with increasing pressure compared to the quartz lattice. Pressure at the time of formation of the minerals is stored as residual stress in the quartz lattice enclosed by the stiff garnet container, which can be quantified using Raman spectroscopy. The stressed quartz lattice results in a shift of the 464 cm^{-1} peak of quartz ($\Delta\upsilon 464$), reflecting the residual confining pressure (Ashley et al., 2016). However, change in garnet composition induces a modification of its elasticity, leading to subsidiary quartz lattice relaxation (Rosenfeld, 1969). Accordingly, we measured garnet compositions near all

297 inclusions. Pressures (P_Q) were then determined using the QuiBCalc program (Ashley et al.,
298 2014b), with the equation of state of Van der Molen and Van Roermund (1986). The
299 program requires three input parameters: 1) the quartz Raman shift ($\Delta\upsilon 464$), 2) the relevant
300 garnet composition, and 3) the temperature of entrapment. Garnet compositions were
301 determined by single spot EMPA near the location of the inclusion or by extrapolation using
302 chemical maps in combination with line scans from EMPA. The individual entrapment
303 temperatures for the inclusions have been carefully calculated by: 1) determining the
304 temperature of the initial stage of garnet growth using pseudosection modeling (Perple_X
305 6.7.3; Connolly, 2005, 1990); 2) considering the previously determined peak temperature of
306 each sample for garnet rim growth (T_C and T_{Zr}) and 3) evaluating the distance of each
307 inclusion from the garnet core and interpolating the temperature linearly from core to rim.
308 The distance to the garnet core of each inclusion was determined using element distribution
309 maps. Quartz inclusions should be small in comparison to the thin section thickness (< 1/3
310 of about 30 μm) and not exposed to the surface or at the bottom of the thin section to ensure
311 good confinement conditions. Only maximum estimates of P_Q were considered, as this value
312 may have been decreased by elastic and viscous relaxation.
313 Peak pressures were also estimated using the phengite barometry based on the
314 assemblage garnet–clinopyroxene–phengite (P_{GOP}), using the equilibrium described in
315 Waters and Martin (1996):
316 6 diopside (Di) + 3 muscovite (Ms) = pyrope (Py) + 2 grossular (Grs) +3 celadonite (Cel) (1)
317 Equilibrium conditions are estimated following the activity models and method of
318 Ravna and Terry (2004), based on transfer reactions between the different end-members.
319 Temperatures estimated through this method, however, essentially rely on Fe-Mg
320 equilibrium (e.g., Ellis and Green, 1979; Ravna, 2000), which is known to overestimate
321 temperatures by about 50 °C (e.g., Klemd et al., 2011; Lü et al., 2009; Nakamura, 2009), and

standard deviations are large (±82 °C and ±65 °C in the quartz and coesite stability fields, respectively), in part due to the unreliable estimation of the Fe^{3+}/Fe_{tot} by charge balance. To circumvent these problems, the peak pressure was herein calculated from independent Zr-in-rutile and RSCM thermometry, since reaction (1) above can be used independently as a phengite geobarometer for a given temperature. To estimate the peak recorded pressure (P_{GOP}), garnet with maximum $\left(a_{grs}^{grt}\right)^2 a_{py}^{grt}$, omphacite with minimum a_{di}^{cpx} (and correspondingly maximum X_{Jd}) and phengite with maximum a_{Al-cel}^{phe} (maximum Si-content) were considered (Carswell et al., 2000; Ravna and Terry, 2004).

4.2 Electron microprobe analyses (EMPA)

Concentration of Zr in rutile was determined by EMPA performed on a JEOL JXA 8900 Superprobe electron microprobe at the Institute for Mineralogy at the Westfälische Wilhelms-Universität Münster. Operating conditions were 15 kV accelerating voltage, 120 nA beam current and a beam diameter of 3 µm. To achieve low detection limits (35 µg/g) of Zr, peak counting rates were 30 s and 15 s for background for Si, Nb and Zr with 5 accumulations. To avoid boundary effects, we measured rutiles >10 µm. We used the quality control after Zack et al. (2004), by measuring the Si concentration, ensuring a maximum limit for the Si content of 250 µg/g.

We performed EMPA to determine the mineral chemistry and chemical zoning of key minerals. Most of the EMPA were performed on a JEOL JXA 8200 Superprobe electron microprobe, equipped with five wavelength-dispersive spectrometers (WDS), at the Freie Universität Berlin, Germany. Some of the analyses were performed on a Cameca SX100 at Camparis in Université Paris 6. Operating conditions were 15 kV accelerating voltage, 20 nA beam current and a beam diameter of 5 µm for white micas, amphiboles and epidotes, and of 1 µm for all other minerals. Both natural and synthetic standards have been used. The

346 raw data were corrected with the ZAF procedure. The relative analytical error for major-
347 elements is less than 1%. Peak counting times are 10 s for Na, Mg, Al, Si, Ca, K, Ti, and Ba,
348 30 s for Mn and Fe, and we used half of the peak time for background counting. Element
349 distribution maps were measured in WDS (Si, Al, Ca, Fe, Mn, Mg, Cr, Ti, Na, K) and
350 energy-dispersive spectrometer mode with an acceleration voltage of 15 kV, a beam current
351 of 20 nA. We used different pixel size (1-10 μm) and dwell time (70-100 ms) depending on
352 the mapped area.

353 *4.3 Raman spectroscopy*

354 Raman spectroscopy has been performed to estimate both pressure and temperature
355 independently. Pressure estimates on quartz inclusions enclosed by garnet were performed at
356 Freie Universität Berlin, Germany using a Horiba ISA Dilor Labram confocal Raman
357 spectrometer, equipped with a Nd-YAG laser (532 nm wavelength) and temperatures on
358 carbonaceous material at École Normale Supérieure, Paris, France using a Renishaw *in Via*
359 equipped with an Ar ion laser (514.5 nm wavelength). Both Raman spectrometers were
360 equipped with a CCD detector and laser spot size was focused to 1 μm through a microscope
361 (x100 objective) on the material of interest. With a 1800 grooves/mm and 100 μm slitwidth
362 the spectral resolution near 464 cm^{-1} was around 4 cm^{-1} for quartz measurements.
363 Calibration was done on a Si standard with a 520.7 cm^{-1} peak in both cases. To ensure good
364 determination of the quartz band, the 464 cm^{-1} band of an additional quartz standard was
365 used. Both standards were measured several times during the measuring period to correct for
366 potential peak shifts with time. To avoid any heating effects on the carbonaceous material
367 due to the laser, the laser energy on the sample surface was reduced to half of its full power
368 by introducing adequate filters. To account for structural heterogeneity of the carbonaceous
369 material, 15-20 spectra were measured for each sample. The spectra obtained with Raman

spectroscopy was processed using the program PeakFit 3.0 (Jandel Scientific) using Voigt functions.

5. Petrological characterization of the HP-UHP unit

We investigated 137 representative samples from various lithologies and metamorphic grades, of which ~30 were selected for petrographic, mineralogical, chemical, and Raman spectroscopic analysis, from the greenschist-facies unit, the HP-UHP unit with both metasedimentary, mafic, and intermediate composition rocks (sub-units 1-4), and the pillow-bearing unit (sub-unit 5). We particularly focused on blueschist- to eclogite-facies rocks to assess peak metamorphic conditions of the studied area and so essentially present below the results obtained for the HP-UHP unit.

The grenschist-facies unit is composed of metasedimentary rocks having experienced greenschist-facies conditions only. These rocks consist of albite + white mica + green amphibole + chlorite + epidote + quartz (Fig. 9a). Titanite, carbonate and iron oxides are present as minor phases. Albite and white mica present a poikiloblastic texture and are elongated parallel to the schistosity. Epidote, chlorite, and green amphibole make up the matrix as patchy small grains. Quartz forms large grains in the matrix. Omphacite, blue amphibole, rutile, and garnet are systematically absent, suggesting peak metamorphism at greenschist-facies conditions. The same mineral assemblage has been determined for samples belonging to the greenschist-facies unit in the south of the belt.

5.1 Mafic rocks

Pure mafic rocks show eclogite-facies conditions and are of two types:

— Blueschists (s.s.) consist of glaucophane (up to 70 vol. %) + garnet ± white mica ± epidote ± quartz ± omphacite (Fig. 9b). Omphacite, when present, is in equilibrium with glaucophane. Garnet porphyroblasts (0.5-1 cm) are euhedral to subhedral. Garnet contains

394 variable amount of inclusions of quartz ± epidote ± omphacite ± amphibole ± chlorite ±
395 carbonate and numerous Ti-phases. Glaucophane composes the matrix as elongated crystals.
396 The Ti-phase is mainly rutile and occasionally titanite. Some samples contain carbonate.
397 Apatite, zircon, and iron oxide represent the accessory minerals.

398 — Eclogites (s.s.) consist of omphacite (up to 80 vol. %) + garnet ± amphibole ±
399 white mica ± epidote ± rutile (Figs. 3c, 9c). Omphacite is mostly interstitial and either
400 patchy or found as rare prisms. Is also occurs as small inclusions in garnets. Garnet occurs
401 as euhedral to subhedral porphyroblasts of 0.5 mm to 3-5 cm size and contains similar
402 inclusions to those of garnets in blueschists (Fig. 9d). Chlorite is commonly found in the
403 core of garnet, epidote is located between the core and mantle, while omphacite is mainly
404 found in the mantle to rim of garnet, suggesting prograde garnet growth. Garnet has often
405 inclusion-free rims (Fig. 9d). Matrix omphacite is anhedral and forms patchy and fibrous
406 grains. When present, matrix amphibole is sub- to euhedral with a prismatic to needle shape.
407 White mica is present as euhedral lamellae. Euhedral rutile occurs as inclusion in garnet,
408 amphibole, white mica, epidote and in the matrix (up to 5%) and is in places rimmed by
409 titanite, when found in the matrix assemblage. Some samples contain carbonate as a minor
410 phase. Accessory minerals include apatite, pyrite, zircon, and iron oxide.

411 *5.2 Volcano-clastic rocks*

412 Volcano-clastic rocks are characterized by a mineral assemblage of white mica +
413 garnet + quartz + albite plus minor and accessory phases such as omphacite, amphibole and
414 epidote. The presence of omphacite, amphibole or epidote shows that these rocks are impure
415 metasediments with a variable psammitic and/or mafic fraction. Garnet size and shape vary
416 significantly among samples, from euhedral to anhedral. The small garnet crystals (0.1-1
417 mm in size) are mostly inclusion free, while the larger porphyroblasts (0.5-1 cm size) show
418 the same inclusion pattern as the more mafic rocks. Volcanoclastic rocks present a more or

less pronounced schistosity (S_n) depeding on the proportion of white mica present in each sample. Albite always displays a poikiloblastic texture.

5.3 Metasedimentary rocks

Metasedimentary rocks are mainly commposed of white mica + garnet + quartz + albite plus minor and accessory phases. Mafic minerals, such as omphacite, amphibole or epidote are absent or present in negligeable proportions. Garnets are often euhedral to subhedral small (0.1-0.2 mm in size) crystals and mostly inclusion free. Metasedimentary rocks always evidence a strong schistosity (S_n), mainly marked by phengite and stretched quartz crystals. Albite displays a poikiloblastic texture.

5.4 Retrograde blueschist-facies to greenschist-facies metamorphism

Blueschist-facies retrogression is indicated by the replacement of omphacite and/or glaucophane by blue-green amphiboles (Fig. 9e), with rare relicts of glaucophane in amphibole cores. Retrogression is also indicated by large (up to 0.5 cm) albite grains (Fig. 9e) and titanite as the main Ti-phase, although a few rutile grains remain in some samples. The greenschist-facies retrogression is marked by further chloritisation of various Mg-Fe-rich minerals such as amphibole, omphacite and garnet (Fig. 9f).

6. Mineral chemistry

Representative analyses of major element composition of minerals are shown in Fig. 10 and given in Table 2 (more data are avalaible in Table S1). Table S2 shows some XRF data of the composition for the different rock types. Mineral abbreviations are after Whitney and Evans (2010).

6.1 Garnet

Garnet is found in all rock types in the HP-UHP unit. Most garnet porphyroblasts show a typical prograde chemical growth zoning, characterized by almandine (Fe) and spessartine (Mn) components decreasing from core to rim, while the pyrope (Mg) and grossular (Ca) components are increasing (Table 2; Fig. 10a). Some samples nevertheless exhibit garnet with different zoning patterns, such as oscillatory zoning, two step growth, or embayments due to corrosion followed by a phase of new garnet growth. The various zonings are not specific to a rock-type. Garnets in eclogite-facies V-type rocks, blueschist-facies V-type rocks, and micaschists samples have an average composition of Alm_{55-82}–Pyr_{1-15}–Grs_{14-41} (except sample FTS 2-7: Alm_{52-63}–Pyr_{14-25}–Grs_{22-25}), Alm_{62-84}–Pyr_{4-15}–Grs_{7-26} and Alm_{60-82}–Pyr_{4-19}–Grs_{6-28}, respectively (Fig. 10a; Table 2). Garnets containing inclusions systematically display a prograde pattern, with greenschists-facies minerals near the core (chlorite) to blueschist-facies minerals (epidote, blue-amphibole) from core to mantle, and eclogite-facies minerals (omphacite, epidote) from mantle to rim. Quartz inclusions are located throughout the whole garnet, while coesite inclusions have been found only in the garnet mantle.

6.2 White mica

White mica occurs as paragonite and/or phengite. They form single euhedral crystals of paragonite and phengite (or an intergrowth) in mafic omphacite, eclogite-facies and retrograde blueschist-facies samples. In pelitic rocks, white mica aligns along the schistosity and forms the matrix. Paragonite and phengite present Na/(K+Na) values of 0.8-1 and 0.1-0.3, respectively. Phengites show Fe+Mg (pfu) values ranging from 0.37 to 0.67 and a Si (pfu) content of 3.25 to 3.70 (Fig. 10b). Offset from the tschermak 1:1 line (Fig. 10b) is likely due to a high Fe^{3+} content. Paragonite displays a Fe (pfu) content ≤ 0.025. Paragonite

464 is found is all rock types and is present as a retrograde phase in eclogites. In greenschist
465 samples, paragonite is the only white mica present.

466 *6.3 Clinopyroxene*

467 Clinopyroxene is classified according to the nomenclature of Morimoto (1988). The
468 estimation of the ferric iron content is based on the method described in Droop (1987). Most
469 of the clinopyroxene minerals are omphacite (Jd_{24-58}–Ae_{0-32}–Di-Hd_{30-62}), except for two
470 samples (eclogites s.s.), which are partly in the field of aegerine-augite (Jd_{21-34}–Ae_{30-36}–Di-
471 Hd_{33-47}) (Fig. 10c; Table 2). Omphacites form a matrix of intergrown patchy grains, due to
472 variation of jadeite and aegerine composition (Fig. 9d). Omphacite occurring as inclusion in
473 garnet and within the matrix display the same compositional range, although inclusions tend
474 to be closer to the aegirine-augite field.

475 *6.4 Amphibole*

476 Amphibole is classified according to the nomenclature of Leake et al. (1997, 2004)
477 (Fig. 10d) and structural formulae are calculated after the procedure outlined by J.
478 Schumacher (in Leake et al., 1997). Amphiboles are mainly glaucophane and barroisite in
479 composition, with minor occurences of winchite, richterite, Mg-hornblendeand rare
480 actinolite (Table 2). They occur as prismatic and acicular euhedral crystals, or as prisms
481 elongated parallel to schistosity. Blue amphibole in eclogites occurs along the Dn+1
482 schistosity or in pressure shadows along Dn. They form porphyroblasts floating in the
483 matrix, as matrix minerals, or as inclusion in other minerals such as garnet. Amphibole
484 retrogression is marked by thin barroisitic or crossitic rims surrounding glaucophane
485 porphyroblasts. Amphibole inclusions in garnet have compositions similar to the matrix
486 minerals.

487 *6.5 Epidote group minerals*

488 Epidote-group minerals occur as prismatic and acicular shape large grains of various
489 sizes in the matrix or as inclusions in garnet. Some epidotes, mainly in mafic samples,
490 contain quartz, rutile and amphibole inclusions. Most matrix epidote-group minerals present
491 a core to rim zoning varying from allanitic or epidotic (LREE- or Fe^{3+}-rich) to clinozoisite
492 (Al^{3+}-rich). In the sample M 14.8 from the greenschist-facies unit, their composition is
493 closer to the clinozoisite end-member, with X_{Al} (Al/(Al+Fe^{3+})) values of 0.7-0.9 (Table 2).

494 *6.6 Chlorite*

495 Chlorite, when present, is commonly associated with garnet and appears in garnet core
496 regions as inclusion, or filling fractures across garnet, or replacing garnet at garnet rims. In
497 retrogressed samples, chlorite is present in the matrix as elongated or patchy crystals. Their
498 X_{Mg} varies between 0.2 and 0.6 in the HP-UHP unit, while chlorite in the greenschist-facies
499 unit has an X_{Mg}=0.64-0.67 (Table 2).

500 *6.7 Rutile/Titanite*

501 In pristine high-pressure rocks, the main Ti-phase is rutile, occurring in the matrix and
502 as inclusion in garnet, white mica, amphibole, epidote. Matrix rutile may develop a titanite
503 rim when significant retrogression affected the rock.

504 *6.8 Other minerals*

505 Carbonate minerals have compositions between ankerite and calcite (Table 2). They
506 occur as vein filling, single crystal in the matrix or as inclusions. Albite (X_{Ab} > 0.98, Table 2)
507 formed during retrogression and is mostly found in mica-rich samples and occasionally in
508 more mafic ones. Pyrite crystals occur as matrix mineral as well as inclusion in various
509 minerals. Apatite is mostly present in the matrix as rounded grains. Zircon is present as rare
510 small grains (few μm).

7. Estimation of peak P-T conditions

7.1 Peak temperature estimates

The thermometer based on graphitization of the carbonaceous material (T_C) could be applied to 24 samples in the HP-UHP unit, mainly V- and S- type, as the M-type rarely contains carbonaceous material, and one sample in the Greenschist Unit (M 14.10; to assess its peak metamorphic condition). The proportion of carbonaceous material varies between a few percent to up to 10-20 % of the mineral assemblage (garnet + carbonaceous material + white mica + quartz ± feldspar ± amphibole ± omphacite). The thermometer based on Zr content in rutile (T_{Zr}) was applied to 10 samples (Table S3). This allows comparison of both thermometers and a temperature estimate for samples lacking carbonaceous material.

Estimated T_C values range between 525 °C and 553 °C (with 15 to 32 °C intra-sample error) with an average of 539 ± 13 °C (Fig. 11a). Two samples exhibit slightly off range T_C estimates of 509 ± 20 °C (AT 14.30) and 573 ± 29 °C (AK 14.10-1), although remaining in the range within error of the method. T_{Zr} estimates display slightly lower values than T_C (Fig. 11a). T_{Zr} estimates range from 520 °C to 543 °C (with 14 to 22 °C intra-sample error), with 530 ± 7 °C on average (Fig. 11a). The combination of both thermometers results in an average temperature of 538 ± 12 °C for the entire HP-UHP unit with a rather homogeneous distribution throughout the studied area (Fig. 11b). No significant difference is observed between samples with distinct apparent metamorphic grade (blueschists, mixed blueschists/eclogites, eclogites; Fig. 11c). Sample M 14.10 exhibits a T_C value of 180 ± 35 °C with a maximum of 235 °C, consistent with maximum low-grade greenschist-facies conditions.

7.2 Pressure estimates

The QuiG barometer was applied to 18 samples from various rock types to estimate minimum values of the peak pressure (P_R) in the HP-UHP unit. Garnets used for QuiG

536 barometry have an average composition of $Alm_{67.8}$-$Sps_{2.4}$-$Pyr_{9.0}$-$Grs_{20.5}$, with core to rim
537 variations ranging between $Alm_{64.9}$-$Sps_{7.1}$-$Pyr_{8.6}$-$Grs_{19.4}$ and $Alm_{63.9}$-$Sps_{2.2}$-$Pyr_{10.0}$-$Grs_{23.4}$.
538 Most garnets present a prograde growth zoning, allowing to correlate the temperature
539 linearily from core to rim for each mineral inclusion. The $\Delta\upsilon 464$ value (and accordingly
540 pressure) increases from garnet core to garnet mantle, with a slight decrease towards the
541 garnet rim (Fig. 11e). Estimated values of P_R vary from 1.5 to 2.8 GPa with an error of 0.2
542 GPa.

543 For the sake of comparison (and for samples lacking suitable quartz inclusions for the
544 QuiG barometry) we applied the phengite barometer (P_{GOP}) to 6 samples in the HP-UHP
545 unit. P_{GOP} values obtained range from 2.3 to 3.0 GPa, with 3 samples exhibiting values
546 above the quartz-coesite transition (>0.6 GPa, Richter et al., 2016).

547 Coesite inclusions in garnet were identified by Raman spectroscopy by their main
548 bands at 521 cm^{-1} (Fig. 11d) and are mainly found in the mantle zone of garnet. The
549 presence of coesite implies a minimum pressure of ~ 2.6 GPa for the determined regional
550 temperature of ~540 °C (Richter et al., 2016). We considered a minimum peak pressure of
551 2.6 GPa for coesite-bearing samples, when the estimated pressure with QuiG (P_R) and/or
552 phengite barometry (P_{GOP}) was < 2.6 GPa.

553 The combination of P_R ,P_{GOP}, and coesite occurrence for each sample provides a new
554 range of minimum peak pressures of 2.1 to 3.0 GPa, with an average of 2.5 ± 0.2 GPa. This
555 restricted pressure range reveals a rather homogeneous distribution throughout the sampled
556 area (Fig. 11e). No variations in pressure are observed across the observed km-scale shear
557 zones (Fig. 12d).

8. Discussion

8.1 Peak metamorphic conditions across the HP-UHP unit

Peak P-T conditions in the HP-UHP unit (Table S4) were investigated on continuously distributed samples across the entire Akeyazi metamorphic complex (AMC), using the same combination of methods.

Peak-temperatures estimated by RSCM spectroscopy, T_C, yielded a tight cluster at ~540 °C (Figs. 11a,b). Only two samples deviate significantly from this average value (AT 14.30, T_C=509 °C and AK 14.10-1, T_C=573 °C) and may record local temperature deviations, possibly as a result of fluid-rock interactions. T_{Zr} yields slightly lower values than T_C, although overlapping within error. Minor Zr diffusion out of rutile grains during cooling may have lowered T_{Zr} estimates (Cherniak, 2000; Zack et al., 2004), which seems supported by the observation of local zircon or baddeleyite exsolutions within rutile. Interestingly, T_{Zr} displays no difference in temperature for eclogites or blueschists (Fig. 11c). This confirms that the distinct mineral assemblages of these rocks reflect individual bulk composition rather than different P-T conditions (e.g., Beinlich et al., 2010; Tian and Wei, 2014).

Estimated pressures, P_R and P_{GOP}, range from 1.48 GPa to 2.81 GPa and 2.31 GPa to 2.98 GPa, respectively. It should be recalled that P_R values determined through the QuiG barometry correspond to minimum estimates of Pmax, since estimated pressures only reflect the residual pressure preserved by the quartz inclusion, whose relaxation in turn depends on the elasticity of its host (Enami, 2012). The discrepancy, in some samples and in the same garnets (e.g., AK 14.66), between very low P_R estimates around 1.5 GPa and the presence of coesite inclusions implying P > 2.6 GPa (Richter et al., 2016), could therefore result from cracks in the vicinity of the measured quartz inclusions (thereby altering quartz relaxation; Angel et al., 2015; Ashley et al., 2014a) or inclusions being located too close to the thin

583 section edge. This is corroborated by the observation of many cracks in garnets, especially
584 the large ones, in addition to a large amount of inclusions very close to each other in many
585 of the garnets. In particular, the dilatant transformation of coesite inclusions to quartz can
586 fracture garnet (Chopin, 1984; Gillet et al., 1984; Van der Molen and Van Roermund, 1986),
587 leading to partial decompression of quartz inclusions. Interestingly, the quartz maximum
588 shift, peak P_R and coesite findings are mainly located in the garnet mantle zone, followed by
589 a slight P_R decrease towards the rim.

590 Pressures estimated using the phengite barometry (P_{GOP}) are calculated based on
591 textural equilibrium between phengite-ompacite-garnet minerals (using only euhedral garnet
592 devoid of rim corrosion to ensure equilibrium between the last growth stage and the matrix
593 minerals). We only considered maximum Si contents of phengite to estimate the peak
594 pressure, as phengite may have recrystallized to lower Si contents during retrogression. Two
595 of the samples recording P_{GOP} >2.6 GPa contain coesite, suggesting that one may rely on this
596 method to estimate pressure conditions if the minerals chosen really grew in equilibrium at
597 peak conditions.

598 Combining T_{Zr} and T_C yields a regional average of ca. 540 °C for the HP-UHP unit,
599 with no significant variations in temperature along and across the area (Figs. 11a, b, 12d).
600 Therefore this indicates that both thermometers seem to record peak temperatures and that
601 Zr concentrations (for T_{Zr}) or carbonaceous material (for T_c) were not affected by later
602 retrogression (e.g., Beyssac et al., 2002), whatever the lithology (mafic, volcanoclastic, or
603 micaschist) and effective bulk composition (Beinlich et al., 2010).

604 The distribution of global effective pressure P_{eff}, taken as the maximum value of
605 pressure estimates (i.e., out of QuiG barometry, phengite barometry and coesite occurrence),
606 is rather uniform though less homogeneous, ranging from 2.1 GPa to 3.0 GPa, with an
607 average of 2.5 GPa (Fig. 11e). The regional average of ca. 2.5 GPa for the given peak

608 temperatures of ca. 540 °C suggests that the whole area had been at a depth close to or at the
609 quartz-coesite transition zone (Fig. 12d), a conclusion supported by the many coesite
610 findings (e.g., Lü et al., 2009; Lü and Zhang, 2012, this study). The values around 2.5-2.8
611 GPa are also in agreement with recent pseudosection modelling in the AMC (Lü et al., 2009,
612 2012a; Soldner et al., 2017; Tan et al., 2017).

613 These results demonstrate that the sub-units of the HP-UHP sequence were subducted
614 and detached from the downgoing slab to form a single nappe stack near peak burial UHP
615 conditions (Fig. 12). The continuous temperature increase from garnet core to garnet rim,
616 and slight pressure decrease from garnet mantle to garnet rim, indicates partial exhumation
617 of this unit at a slightly higher level, while heating up to 540 °C.

618

619 8.2 Tectonic implications at the scale of the area

620 *8.2.1 Nature and origin of the lithologies*

621 Detailed mapping reveals that the HP-UHP unit is composed of a ~4–5 km-thick
622 metasedimentary and metavolcanoclastic sequence grading southward from more pelitic to
623 more mafic (Fig. 4b). The N-MORB, E-MORB, OIB and/or arc geochemical signatures of
624 the mafic rocks (Gao et al., 1995; Gao and Klemd, 2003; Liu et al., 2014; van der Straaten et
625 al., 2012) testify the existence of a complex oceanic crust (i.e., with seamount-like
626 heterogeneities and/or subduction related arc-volcanism), while metasedimentary
627 components (carbonates and micaschists) may correspond to the sedimentary cover of the
628 subducting oceanic crust and/or trench or fore-arc basin sediments (Ai et al., 2006; Gao et
629 al., 1995; Liu et al., 2014; Meyer et al., 2016).

630 Intercalated radiolarian cherts, pillow basalts and pillow breccias (with N-MORB to E-
631 MORB signature; Gao et al., 1995) of the southernmost and last accreted unit (sub-unit 5)

represent the upper portion of the oceanic slab. We suggest that the north to south lithological and compositional gradient documented here (in sub-units 1 to 4; Figs. 5, 6) reflects the incorporation of increasing amounts of trench material of volcanoclastic origin (likely upper plate derived, for example as a result of large volcanic eruptions; Kutterolf et al., 2008a, 2008b; Scudder et al., 2009) as the subduction system evolves.

This increasing input of volcanoclastic material may also reflect an evolution from subduction accretion (with only thin veneers of deep-sea sediments, as in sub-unit 1, making their way into subduction) to subduction erosion: the more psammitic and mafic components would correspond to large pieces of the accretionary prism and arc-derived material shovelled into subduction. Such an evolution was suggested for the Apennines to explain the change in slope basin deposits and the removal of the toe of the Ligurian accretionary prism (Remitti et al., 2011) and subduction erosion was previously proposed for the AMC (Ai et al., 2006; Liu et al., 2014).

8.2.2 Tectonic mélange or sub-belt model?

Two contradictory concepts were so far proposed for the structural evolution of the AMC (Fig. 1b).

On the one hand, the AMC was regarded as a block in matrix tectonic mélange, assuming eclogite boudins and bodies are embedded in "country rock" metapelites (e.g., Klemd et al., 2015, 2011; Li et al., 2016; Meyer et al., 2016). Our findings conflict with such a mélange structure, as mapping reveals km-scale lateral continuities and interlayering of mafic and sedimentary rocks (Figs.4, 5; see also Gao and Klemd, 2003; Liu et al., 2014). Some rocks (mostly from loose blocks and/or river beds in fact) seem to have experienced a complex P-T evolution (e.g., Li et al., 2016). This could tentatively be reconciled with our findings by thinking these may have been incorporated between tectonic slices, i.e. along major shear zones of the nappe stack.

On the other hand, the AMC was described as consisting of two units: a ultra-high-pressure unit to the North, separated from a high-pressure unit in the South by a ~10-15 km shear zone (Lü et al., 2012a; Tian and Wei, 2014). The lack of pressure gradient across the area (Figs. 11e, 12d), and across a particular contact, does not support the existence of this boundary (which was progressively shifted on the maps, as more and more coesite was discovered in the area; Lü et al., 2012a; Tian and Wei, 2014 and references therein).

Overall, the intimate layering, homogeneous peak P-T estimates (irrespective of sedimentary or mafic protoliths) and almost ubiquitous coesite occurrences throughout the entire study area stand in contradiction with both concepts. Contrary to earlier suggestions (e.g., Klemd et al., 2011; Lü et al., 2012a; Tian and Wei, 2014), large-scale shear zones do not separate units or individual blocks from various depths (Fig. 12a), , but rather accomodate deep stacking and minor later offsets during exhumation.

8.2.3 Succession and significance of deformation stages

Five stages of deformation were identified, the first one being only identified in thin section (D_{n-1}) as quartz inclusion trails in garnet (Figs. 6g, 8f. Garnets enclosing S_{n-1} exhibit prograde growth zoning and preserve increasing pressures from core to rim (P_R), suggesting that this deformation stage developed during burial. The pervasive, dominant schistosity S_n (stage D_n) strikes approximately E-W. A similar ~ENE-WSW trend was reported from a few scattered schistosity measurements in the study of Tian and Wei (2013). Soldner et al. (2017) recently reported foliation and schistosity measurements with (i) a chaotic ENE-WSW trend in Atantayi, (ii) an E-W striking trend north of Kebuerte turning into (iii) a NW-SE trend towards the South.

Later D_{n+1} to D_{n+3} fabrics show very homogeneous N-S trending lineations with top to the north shear senses (Fig. 7k,l). These fabrics (Fig. 12a) are consistent with expected exhumation dynamics following northward subduction (Scheltens et al., 2015; Soldner et al.,

682 2017). D_n and D_{n+1} likely occurred at eclogite-facies conditions, prior to retrograde
683 blueschist-facies conditions. D_{n+2} reflects exhumation at blueschist-facies conditions, as
684 shown by the ubiquitous glaucophane lineations along (mm- to km-scale) shear planes (Fig.
685 7j). Blue- and green-amphibole lineations associated to C' planes (i.e., extensional
686 crenulation cleavage; D_{n+3}) suggest exhumation from blueschist- to greenschist-facies
687 conditions.

688 *8.2.4 Juxtaposition of the HP-UHP unit with other units*

689 The northern greenschist-facies (GS) unit is bound in the North by the south Central
690 Tianshan Suture (e.g., Gao et al., 1999) and in the South by the greenschist/high-pressure
691 detachment (GHPD; this study). This study reappraises the location of the GHPD slightly
692 further to the North with respect to former ones.

693 While the distinction between the HP-UHP unit and the GS unit is sharp in the West, it
694 is less clear in the East, as samples close and on either side of the contact may contain
695 garnet. We propose that the GHPD is more diffuse in the East because it branches into
696 several fault strands. The eclogite sample located immediately north of the GHPD (AK
697 15.20), with T_C ~544°C, would thus represent a tectonic sliver sheared off the HP-UHP unit
698 along the contact during the juxtaposition of the two units. Contrary to Gao et al. (1999),
699 describing greenschist-facies rocks as "country rocks" containing garnet and muscovite and
700 possibly retrogressed from higher pressure conditions, only typical low-grade mineral
701 assemblages and peak temperatures < 250°C were indeed found in this study.

702 In the central part of the GS unit a unit comprising unmetamorphosed and mostly
703 undeformed sedimentary rocks unconformably overlains the GHPD. No age constraints
704 could be obtained, unfortunately, for what was likely a small molasse-type continental basin.

705 8.3 Geodynamic evolution of the southern Chinese Tianshan metamorphic belt

706 Using the above petrological and structural constraints, we tentatively reappraise the
707 geodynamic evolution of the southern Chinese Tianshan metamorphic belt (Fig. 12).

708 *8.3.1 Initial stage: ongoing subduction*

709 The nature of the AMC material indicates that trench infill, during subduction
710 (whether or not an accretionary wedge developed), comprised pelitic and carbonate-rich
711 sediments and variable amounts of volcanoclastic material. Based on (i) the observed
712 lithological gradient from more pelitic in the north to more volcano-clastic and mafic
713 towards the south, (ii) assuming northward subduction (see Geological setting) and
714 recognizing that (iii) the 4-5 km thick sequence is made of a stack of (successive) tectonic
715 slices, it may be argued that pelitic rocks in the north were incorporated first in the
716 subduction zone and that the nature of the original material evolved slightly over time,
717 comprising more volcanic fragments/ashes (Fig. 12a).

718 *8.3.2 Detachment and accretion*

719 Pieces dragged down into subduction get sequentially detached and stacked at
720 eclogite-facies HP-UHP conditions, with average peak pressures around 2.5-2.7 GPa (Fig.
721 12b). This is supporting the existence of a critical point at ca. 80 km depth (Agard et al.,
722 2009) and of coupling/decoupling level from numerical models (e.g., Syracuse et al., 2010;
723 Wada and Wang, 2009). We suggest that the observed sequence was detached and stacked
724 as several slices. The first slice comprises more metapelitic trench infill material, possibly
725 from a still sediment-dominated margin. Successively detached slices reflect the continuous
726 incorporation of an increasing volcano-clastic component into the trench, as a result of
727 subduction erosion and/or increased volcanic activity (Agard et al., 2018; see discussion in §

728 6.2.1). The detachment of each slice is associated with thrust contacts now bounding the
729 structural sub-units observed in the field (Figs. 12a,b). Although residing at ca. 80 km depth,
730 temperatures were buffered and the HP-UHP unit remained relatively cool. This absence of
731 significant heating after peak burial might be explained by shielding of the AMC from heat
732 transfer from the overlying mantle (e.g., fluid circulation along the plate interface or
733 presence of a mantle wedge "cold nose"; Abers et al., 2006; Bayet et al., 2018; van der
734 Straaten et al., 2008).

735 Detachment and stacking of the last tectonic slice with abundant pillow basalts (i.e.,
736 sub-unit 5; Fig. 6f) remains enigmatic, as no peak pressure could be estimated for these
737 rocks (Figs. 11e, 12d): this tectonic slice was either detached from the slab at UHP
738 conditions, or later accreted to the rest of the sequence at eclogitic yet not UHP conditions.

739 Since the GS facies unit did not experience any HP-LT metamorphism, juxtaposition
740 between the HP-UHP and GS units occured late or even postdated the subduction history.
741 Despite the lithological homogeneity of the GS unit and the fact that it is only underlain by
742 HP-LT sub-units, its paleogeographic significance and whether it was subducted is still
743 unclear.

744 *8.3.3 Exhumation*

745 Exhumation and pervasive thinning of the HP-UHP sequence occurred at blueschist-
746 facies conditions, as indicated by ubiquitous glaucophane lineations, most likely through the
747 reactivation of the former thrusts as shear zones (Fig. 12c). As only top to the north shear
748 senses are observed and given the inferred northward subduction, this means that (i) shear
749 zones are extensional (at least in a relative sense) and exhumation-related, and (ii) because
750 they separate units with slightly contrasting lithological content they may have corresponded
751 to the original (thrust) boundaries between the tectonic slices.

From that stage onwards the nappe stack behaved as a single unit, which is supported by the homogeneous distribution of the peak P-T values throughout the entire area (Fig. 12d). Sub-unit 5, if not yet part of the nappe stack (see above), most likely was detached by then from the descending slab, welded and exhumed together with the HP-UHP sequence.

8.3.4 Present day configuration

The greenschist unit was either exhumed prior to exhumation of the HP-UHP unit or coevally, yet, during ongoing subduction. In both cases, the AMC developed a dome-like structure with the GS unit on top of the HP-UHP unit and 'detachment' faults on each side. This metamorphic dome may have formed while the UHP unit was exhumed throughout the greenschist unit, as in metamorphic core-complexes (e.g., Jolivet et al., 1998), or may represent later folding of previously exhumed units. Owing to the lack of diagnostic shape for the exhumation P-T path in support of the first hypothesis, folding is most likely postdating much of the exhumation. Both units were later tilted and subsequently eroded. A small molasse basin formed on top of the GHPD after all metamorphic units had reached the surface, and was later squeezed during (possibly Cenozoic) compression (Fig. 12d).

9. Conclusions

The systematic study of structural and lithological relationships tied to peak P-T estimates across the whole Southern Tianshan metamorphic belt allows to draw the following conclusions:

1. The lithology in the HP-UHP unit exhibits a north to south gradient, from more pelitic to more mafic. This is thought to reflect an increasing amount of volcanoclastic component in subducted material and/or a shift to subduction erosion mode through time. The studied area does not represent a block-in-matrix

tectonic mélange, as continuous layers of mafic rocks are intimately interlayered with metapelitic layers.

2. The HP-UHP unit underwent rather homogeneous peak P-T conditions around ~2.5 GPa and ~540 °C and reached uniform UHP or near UHP conditions, as attested by the ubiquitous presence of coesite. Subducted trench infill was thus detached at HP-UHP conditions and stacked as several individual tectonic slices (sub-units 1-4) to form the present-day nappe stack.
3. Pervasive deformation occurs in the HP-UHP unit through five deformation stages: (i) Dn-1 records burial and is only visible at mm-scale as inclusion trails in garnet; (ii) Dn is represented by the penetrative north dipping schistosity striking ~ENE-WSW and most likely coincides with the nappe stacking of the sub-units recognized in this study (i.e., initial thrust contacts); (iii) Dn+1, corresponds to the eclogite to blueschist-facies crenulation and folding of the schistosity; (iv) Dn+2 is marked by distributed blueschist-facies shearing during exhumation and is reworking earlier, large-scale shear zones as extensional structures; (v) Dn+3 is characterized by ductile to brittle C' structures locally cutting across all previous structures.
4. No gap in peak pressure or temperature is observed across the large-scale shear zones operating during retrograde blueschist-facies conditions. This observation suggest that they separate sub-units stacked at similar depths and accomodate only minor offsets during later exhumation.
5. Progressive deformation patterns in the area are consistent with a northward dipping subduction. The HP-UHP sequence was exhumed close to the surface and juxtaposed to the greenschist facies unit during or after its exhumation.

Acknowledgements

We thank Laura Airaghi for helpful comments and acknowledge Ralf Milke, Jasper Berndt-Gerdes and Anja Maria Schleicher for electron microprobe and XRF analyses. We also want to thank the reviewers , Davide Zanoni, and Thomas Pettke for their comments and suffestions to revise this manuscript. This research received funding from the People Programme (Marie Curie Actions) of the European Union's Seventh Framework Programme FP7/2017–2013/under REA grant agreement no. 604713, 'Zooming in between Plates (ZIP)'.

References

Abers, G.A., van Keken, P.E., Kneller, E.A., Ferris, A., Stachnik, J.C., 2006. The thermal structure of subduction zones constrained by seismic imaging: Implications for slab dehydration and wedge flow. Earth Planet. Sci. Lett. 241, 387–397. https://doi.org/10.1016/j.epsl.2005.11.055

Agard, P., Plunder, A., Angiboust, S., Bonnet, G., Ruh, J., 2018. The subduction plate interface : rock record and mechanical coupling (from long to short timescales). LITHOS 321, 537–561.

Agard, P., Yamato, P., Jolivet, L., Burov, E., 2009. Exhumation of oceanic blueschists and eclogites in subduction zones: Timing and mechanisms. Earth-Science Rev. 92, 53–79. https://doi.org/10.1016/j.earscirev.2008.11.002

Ai, Y., Zhang, L., Li, X., Qu, J., 2006. Geochemical characteristics and tectonic implications of HP-UHP eclogites and blueschists in Southwestern Tianshan, China. Prog. Nat. Sci. 16, 624–632. https://doi.org/10.1080/10020070612330044

Angel, R.J., Nimis, P., Mazzucchelli, M.L., Alvaro, M., Nestola, F., 2015. How large are departures from lithostatic pressure? Constraints from host-inclusion elasticity. J.

824 Metamorph. Geol. 33, 801–813. https://doi.org/10.1111/jmg.12138
825 Angiboust, S., Agard, P., 2010. Initial water budget: The key to detaching large volumes of
826 eclogitized oceanic crust along the subduction channel? Lithos 120, 453–474.
827 https://doi.org/10.1016/j.lithos.2010.09.007
828 Angiboust, S., Agard, P., Jolivet, L., Beyssac, O., 2009. The Zermatt-Saas ophiolite: The
829 largest (60-km wide) and deepest (c. 70-80km) continuous slice of oceanic lithosphere
830 detached from a subduction zone? Terra Nov. 21, 171–180.
831 https://doi.org/10.1111/j.1365-3121.2009.00870.x
832 Ashley, K.T., Caddick, M.J., Steele-MacInnis, M.J., Bodnar, R.J., Dragovic, B., 2014a.
833 Geothermobarometric history of subduction recorded by quartz inclusions in garnet.
834 Geochemistry, Geophys. Geosystems 15, 350–360.
835 https://doi.org/10.1002/2013GC005106
836 Ashley, K.T., Steele-MacInnis, M., Bodnar, R.J., Darling, R.S., 2016. Quartz-in-garnet
837 inclusion barometry under fire: Reducing uncertainty from model estimates. Geology
838 44, 699–702. https://doi.org/10.1130/G38211.1
839 Ashley, K.T., Steele-MacInnis, M., Caddick, M.J., 2014b. QuIB Calc: A MATLAB®script
840 for geobarometry based on Raman spectroscopy and elastic modeling of quartz
841 inclusions in garnet. Comput. Geosci. 66, 155–157.
842 https://doi.org/10.1016/j.cageo.2014.01.005
843 Bayet, L., John, T., Agard, P., Gao, J., Li, J., 2018. Massive sediment accretion at ~ 80 km
844 depth along the subduction interface : Evidence from the southern Chinese Tianshan.
845 https://doi.org/https://doi.org/10.1130/G40201.1
846 Bebout, G.E., 2007. Metamorphic chemical geodynamics of subduction zones. Earth Planet.
847 Sci. Lett. 260, 373–393. https://doi.org/10.1016/j.epsl.2007.05.050
848 Bebout, G.E., Agard, P., Kobayashi, K., Moriguti, T., Nakamura, E., 2013. Devolatilization

849 history and trace element mobility in deeply subducted sedimentary rocks: Evidence
850 from Western Alps HP/UHP suites. Chem. Geol. 342, 1–20.
851 https://doi.org/10.1016/j.chemgeo.2013.01.009
852 Bebout, G.E., Penniston-Dorland, S.C., 2016. Fluid and mass transfer at subduction
853 interfaces-The field metamorphic record. Lithos 240–243, 228–258.
854 https://doi.org/10.1016/j.lithos.2015.10.007
855 Beinlich, A., Klemd, R., John, T., Gao, J., 2010. Trace-element mobilization during Ca-
856 metasomatism along a major fluid conduit: Eclogitization of blueschist as a
857 consequence of fluid-rock interaction. Geochim. Cosmochim. Acta 74, 1892–1922.
858 Beyssac, O., Goffé, B., Chopin, C., Rouzaud, J.N., 2002. Raman spectra of carbonaceous
859 material in metasediments: A new geothermometer. J. Metamorph. Geol. 20, 859–871.
860 https://doi.org/10.1046/j.1525-1314.2002.00408.x
861 Carswell, D.A., Wilson, R.N., Zhai, M., 2000. Metamorphic evolution, mineral chemistry
862 and thermobarometry of schists and orthogneisses hosting ultra-high pressure eclogites
863 in the Dabieshan of central China. Lithos 52, 121–155. https://doi.org/10.1016/S0024-
864 4937(99)00088-2
865 Charvet, J., Shu, L., Laurent-Charvet, S., Wang, B., Faure, M., Cluzel, D., Chen, Y., De
866 Jong, K., 2011. Palaeozoic tectonic evolution of the Tianshan belt, NW China. Sci.
867 China Earth Sci. 54, 166–184.
868 Chen, K., Gumiaux, C., Augier, R., Chen, Y., Wang, Q., Lin, W., Wang, S., 2011. The
869 Mesozoic palaeorelief of the northern Tian Shan (China). Terra Nov. 23, 195–205.
870 Cherniak, D.J., 2000. Pb diffusion in rutile. Contrib. to Mineral. Petrol. 139, 198–207.
871 https://doi.org/10.1007/PL00007671
872 Chopin, C., 2003. Ultrahigh-pressure metamorphism: Tracing continental crust into the
873 mantle. Earth Planet. Sci. Lett. 212, 1–14. https://doi.org/10.1016/S0012-

821X(03)00261-9

Chopin, C., 1984. Coesite and pure pyrope in high-grade blueschists of the Western Alps: a first record and some consequences. Contrib. to Mineral. Petrol. 86, 107–118. https://doi.org/10.1007/BF00381838

Chopin, C., Henry, C., Michard, A., 1991. Geology and petrology of the coesite-bearing terrain, Dora Maira massif, Western Alps. Eur. J. Mineral. 3, 263–291.

Clift, P., Vannucchi, P., 2004. Controls on tectonic accretion versus erosion in subduction zones: Implications for the origin and recycling of the continental crust. Rev. Geophys. 42. https://doi.org/10.1029/2003RG000127

Cloos, M., Shreve, R.L., 1996. Shear-zone thickness and the seismicity of Chilean- and Marianas-type subduction zones. Geology 24, 107–110. https://doi.org/10.1130/0091-7613(1996)024<0107:SZTATS>2.3.CO;2

Cloos, M., Shreve, R.L., 1988a. Subduction-Channel Model of Prism Accretion, Melange Formation, Sediment Subduction, and Subduction Erosion at Convergent Plate Margins: 2. Implications and Discussion. Pure Appl. Geophys. PAGEOPH 128, 501–545. https://doi.org/10.1007/BF00874548

Cloos, M., Shreve, R.L., 1988b. Subduction-Channel Model of Prism Accretion , Melange Formation , Sediment Subduction , and Subduction Erosion at Convergent Plate Margins : 1 . Background and Description. Pure Appl. Geophys. PAGEOPH 128, 455–500.

Connolly, J.A.D., 2005. Computation of phase equilibria by linear programming: A tool for geodynamic modeling and its application to subduction zone decarbonation. Earth Planet. Sci. Lett. 236, 524–541. https://doi.org/10.1016/j.epsl.2005.04.033

Connolly, J.A.D., 1990. Multivariable phase diagrams: an algorithm based on generalized thermodynamics. Am. J. Sci. 290, 666–718.

899 Droop, G.T.R., 1987. A General Equation for Estimating Fe3+ Concentrations in
900 Ferromagnesian Silicates and Oxides from Microprobe Analyses, Using Stoichiometric
901 Criteria. Mineral. Mag. 51, 431–435. https://doi.org/10.1180/minmag.1987.051.361.10
902 Ellis, D.J., Green, D.H., 1979. An experimental study of the effect of Ca upon garnet-
903 clinopyroxene Fe-Mg exchange equilibria. Contrib. to Mineral. Petrol. 71, 13–22.
904 https://doi.org/10.1007/BF00371878
905 Enami, M., 2012. Influence of garnet hosts on the Raman spectra of quartz inclusions. J.
906 Mineral. Petrol. Sci. 107, 173–180. https://doi.org/10.2465/jmps.111216
907 Enami, M., Nishiyama, T., Mouri, T., 2007. Laser Raman microspectrometry of
908 metamorphic quartz: A simple method for comparison of metamorphic pressures. Am.
909 Mineral. 92, 1303–1315. https://doi.org/10.2138/am.2007.2438
910 Festa, A., Dilek, Y., Pini, G.A., Codegone, G., Ogata, K., 2012. Mechanisms and processes
911 of stratal disruption and mixing in the development of mélanges and broken
912 formations: Redefining and classifying mélanges. Tectonophysics 568–569, 7–24.
913 https://doi.org/10.1016/j.tecto.2012.05.021
914 Gao, J., He, G., Li, M., Xiao, X., Tang, Y., Wang, J., Zhao, M., 1995. The mineralogy,
915 petrology, metamorphic PTDt trajectory and exhumation mechanism of blueschists,
916 south Tianshan, northwestern China. Tectonophysics 250, 151–168.
917 Gao, J., Klemd, R., 2003. Formation of HP-LT rocks and their tectonic implications in the
918 western Tianshan Orogen, NW China: geochemical and age constraints. Lithos 66, 1–
919 22.
920 Gao, J., Klemd, R., 2001. Primary fluids entrapped at blueschist to eclogite transition:
921 evidence from the Tianshan meta-subduction complex in northwestern China. Contrib.
922 to Mineral. Petrol. 142, 1–14.
923 Gao, J., Klemd, R., 2000. Eclogite Occurrences in the Southern Tianshan High-Pressure

924 Belt, Xinjiang, Western China. Gondwana Res. 3, 33–38.
925 Gao, J., Li, M., Xiao, X., Tang, Y., He, G., 1998. Paleozoic tectonic evolution of the
926 Tianshan Orogen, northwestern China. Tectonophysics 287, 213–231.
927 Gao, J., Long, L., Klemd, R., Qian, Q., Liu, D., Xiong, X., Su, W., Liu, W., Wang, Y.,
928 Yang, F., 2009. Tectonic evolution of the South Tianshan orogen and adjacent regions,
929 NW China: geochemical and age constraints of granitoid rocks. Int. J. Earth Sci. 98,
930 1221–1238.
931 Gao, Klemd, Zhang, Wang, Xiao, 1999. P–T path of high-pressure/low-temperature rocks
932 and tectonic and implications in the western Tianshan Mountains and NW China. J.
933 Metamorph. Geol. 17, 621–636.
934 Gillet, P., Ingrin, J., Chopin, C., 1984. Coesite in subducted continental crust: P-T history
935 deduced from an elastic model. Earth Planet. Sci. Lett. 70, 426–436.
936 https://doi.org/10.1016/0012-821X(84)90026-8
937 Grigull, S., Krohe, A., Moos, C., Wassmann, S., Stöckhert, B., 2012. “Order from chaos”: A
938 field-based estimate on bulk rheology of tectonic mélanges formed in subduction
939 zones. Tectonophysics 568–569, 86–101. https://doi.org/10.1016/j.tecto.2011.11.004
940 Guillot, S., Hattori, K., Agard, P., Schwartz, S., Vidal, O., 2009. Exhumation processes in
941 oceanic and continental subduction context. Springer Berlin Heidelberg.
942 https://doi.org/10.1007/978-3-540-87974-9
943 Han, B.-F., He, G.-Q., Wang, X.-C., Guo, Z.-J., 2011. Late Carboniferous collision between
944 the Tarim and Kazakhstan–Yili terranes in the western segment of the South Tian Shan
945 Orogen, Central Asia, and implications for the Northern Xinjiang, western China.
946 Earth-Science Rev. 109, 74–93.
947 Hegner, E., Klemd, R., Kröner, A., Corsini, M., Alexeiev, D. V., Iaccheri, L.M., Zack, T.,
948 Dulski, P., Xia, X., Windley, B.F., 2010. Mineral ages and p-t conditions of late

949 paleozoic high-pressure eclogite and provenance of mélange sediments from atbashi in
950 the south tianshan orogen of kyrgyzstan. Am. J. Sci. 310, 916–950.
951 https://doi.org/10.2475/09.2010.07
952 Jahn, B., Wu, F., Chen, B., 2000. Granitoids of the Central Asian Orogenic Belt and
953 continental growth in the Phanerozoic. Trans. R. Soc. Edinb. Earth Sci. 91, 181–193.
954 John, T., Gussone, N., Podladchikov, Y.Y., Bebout, G.E., Dohmen, R., Halama, R., Klemd,
955 R., Magna, T., Seitz, H.M., 2012. Volcanic arcs fed by rapid pulsed fluid flow through
956 subducting slabs. Nat. Geosci. 5, 489–492. https://doi.org/10.1038/ngeo1482
957 John, T., Scherer, E.E., Schenk, V., Herms, P., Halama, R., Garbe-Schönberg, D., 2010.
958 Subducted seamounts in an eclogite-facies ophiolite sequence: The Andean Raspas
959 Complex, SW Ecuador. Contrib. to Mineral. Petrol. 159, 265–284.
960 https://doi.org/10.1007/s00410-009-0427-0
961 Jolivet, L., Daniel, J.M., Truffert, C., Goffé, B., 1994. Exhumation of deep crustal
962 metamorphic rocks and crustal extension in arc and back-arc regions. Lithos 33, 3–30.
963 https://doi.org/10.1016/0024-4937(94)90051-5
964 Klemd, R., Bröcker, M., Hacker, B.R., Gao, J., Gans, P., Wemmer, K., 2005. New Age
965 Constraints on the Metamorphic Evolution of the High-Pressure/Low-Temperature Belt
966 in the Western Tianshan Mountains, NW China. J. Geol. 113, 157–168.
967 https://doi.org/10.1086/427666
968 Klemd, R., Gao, J., Li, J.L., Meyer, M., 2015. Metamorphic evolution of (ultra)-high-
969 pressure subduction-related transient crust in the South Tianshan Orogen (Central
970 Asian Orogenic Belt): Geodynamic implications. Gondwana Res. 28, 1–25.
971 https://doi.org/10.1016/j.gr.2014.11.008
972 Klemd, R., John, T., Scherer, E.E., Rondenay, S., Gao, J., 2011. Changes in dip of
973 subducted slabs at depth: Petrological and geochronological evidence from HP-UHP

974 rocks (Tianshan, NW-China). Earth Planet. Sci. Lett. 310, 9–20.
975 Klemd, R., Schröter, F.C., Will, T.M., Gao, J., 2002. P–T evolution of glaucophane–
976 omphacite bearing HP–LT rocks in the western Tianshan Orogen, NW China: new
977 evidence for “Alpine-type” tectonics. J. Metamorph. Geol. 20, 239–254.
978 Kutterolf, S., Freundt, A., Peréz, W., 2008a. Pacific offshore record of plinian arc volcanism
979 in Central America: 2. Tephra volumes and erupted masses. Geochemistry, Geophys.
980 Geosystems 9, n/a-n/a. https://doi.org/10.1029/2007GC001791
981 Kutterolf, S., Freundt, A., Peréz, W., Mörz, T., Schacht, U., Wehrmann, H., Schmincke, H.-
982 U., 2008b. Pacific offshore record of plinian arc volcanism in Central America: 1.
983 Along-arc correlations. Geochemistry, Geophys. Geosystems 9, n/a-n/a.
984 https://doi.org/10.1029/2007GC001631
985 Kylander-clark, A.R.C., Hacker, B.R., Mattinson, C.G., 2012. Size and exhumation rate of
986 ultrahigh-pressure terranes linked to orogenic stage. Earth Planet. Sci. Lett. 321–322,
987 115–120. https://doi.org/10.1016/j.epsl.2011.12.036
988 Laurent, V., Jolivet, L., Roche, V., Augier, R., Scaillet, S., Cardello, G.L., 2016. Strain
989 localization in a fossilized subduction channel: Insights from the Cycladic Blueschist
990 Unit (Syros, Greece). Tectonophysics 672–673, 150–169.
991 https://doi.org/10.1016/j.tecto.2016.01.036
992 Lázaro, C., García-Casco, A., Rojas Agramonte, Y., Kröner, A., Neubauer, F., Iturralde-
993 Vinent, M., 2009. Fifty-five-million-year history of oceanic subduction and exhumation
994 at the northern edge of the Caribbean plate (Sierra del Convento mélange, Cuba). J.
995 Metamorph. Geol. 27, 19–40. https://doi.org/10.1111/j.1525-1314.2008.00800.x
996 Leake, B., Woolley, A.R., Arps, C.E.S., Birch, W.D., Gilbert, C.M., Grice, J.D., Hawthorne,
997 F.C., Kato, A., Kisch, H.J., Krivovichev, V.G., Linthout, K., Laird, J., Mandarino, J.A.,
998 Maresch, W. V., Nickel, E.H., Rock, N.M.S., Schumacher, J.C., Smith, D.C.,

999 Stephenson, N.C.N., Ungaretti, L., Whittaker, E.J.W., Youzhi, G., 1997. Nomenclature
1000 of Amphiboles: Report of the Subcommittee on Amphiboles of the International
1001 Mineralogical Association Commission on New Minerals and Mineral Names. Can.
1002 Mineral. 35, 1571–1606.
1003 https://doi.org/https://doi.org/10.1180/minmag.1997.061.405.13
1004 Leake, B.E., Woolley, A.R., Birch, W.D., Burke, E.A.J., Ferraris, G., Grice, J.D.,
1005 Hawthorne, F.C., Kisch, H.J., Krivovichev, V.G., Schumacher, J.C., Stephenson,
1006 N.C.N., Whittaker, E.J.W., 2004. Nomenclature of amphiboles: Additions and revisions
1007 to the International Mineralogical Association's amphibole nomenclature. Am.
1008 Mineral. 89, 883–887. https://doi.org/10.2113/gscanmin.41.6.1355
1009 Li, J.L., Klemd, R., Gao, J., John, T., 2016. Poly-cyclic metamorphic evolution of eclogite:
1010 Evidence for multistage burial-exhumation cycling in a subduction channel. J. Petrol.
1011 57, 119–146. https://doi.org/10.1093/petrology/egw002
1012 Li, J.L., Klemd, R., Gao, J., Meyer, M., 2012. Coexisting carbonate-bearing eclogite and
1013 blueschist in SW Tianshan, China: Petrology and phase equilibria. J. Asian Earth Sci.
1014 60, 174–187. https://doi.org/10.1016/j.jseaes.2012.08.015
1015 Liou, J.G., Tsujimori, T., Yang, J., Zhang, R.Y., Ernst, W.G., 2014. Recycling of crustal
1016 materials through study of ultrahigh-pressure minerals in collisional orogens,
1017 ophiolites, and mantle xenoliths: A review. J. Asian Earth Sci. 96, 386–420.
1018 Liou, J.G., Tsujimori, T., Zhang, R.Y., Katayama, I., Maruyama, S., 2004. Global UHP
1019 Metamorphism and Continental Subduction/Collision: The Himalayan Model. Int.
1020 Geol. Rev. 46, 1–27. https://doi.org/10.2747/0020-6814.46.1.1
1021 Liu, X., Su, W., Gao, J., Li, J., Jiang, T., Zhang, X., Ge, X., 2014. Paleozoic subduction
1022 erosion involving accretionary wedge sediments in the South Tianshan Orogen:
1023 Evidence from geochronological and geochemical studies on eclogites and their host

metasediments. Lithos 210, 89–110. https://doi.org/10.1016/j.lithos.2014.09.017

Long, L., Gao, J., Klemd, R., Beier, C., Qian, Q., Zhang, X., Wang, J., Jiang, T., 2011. Geochemical and geochronological studies of granitoid rocks from the Western Tianshan Orogen: Implications for continental growth in the southwestern Central Asian Orogenic Belt. Lithos 126, 321–340.

Lü, Z., Bucher, K., Zhang, L., Du, J., 2012a. The Habutengsu metapelites and metagreywackes in western Tianshan, China: Metamorphic evolution and tectonic implications. J. Metamorph. Geol. 30, 907–926. https://doi.org/10.1111/j.1525-1314.2012.01002.x

Lü, Z., Zhang, L., 2012. Coesite in the eclogite and schist of the Atantayi Valley, southwestern Tianshan, China. Chinese Sci. Bull. 57, 1467–1472.

Lü, Z., Zhang, L., Du, J., Bucher, K., 2009. Petrology of coesite-bearing eclogite from Habutengsu Valley, western Tianshan, NW China and its tectonometamorphic implication. J. Metamorph. Geol. 27, 773–787.

Lü, Z., Zhang, L., Du, J., Yang, X., Tian, Z., Xia, B., 2012b. Petrology of HP metamorphic veins in coesite-bearing eclogite from western Tianshan, China: Fluid processes and elemental mobility during exhumation in a cold subduction zone. Lithos 136–139, 168–186. https://doi.org/10.1016/j.lithos.2011.10.011

Luoni, P., Rebay, G., Spalla, M.I., Zanoni, D., 2018. UHP Ti-chondrodite in the Zermatt-Saas serpentinite: Constraints on a new tectonic scenario.

Marschall, H.R., Schumacher, J.C., 2012. Arc magmas sourced from mélange diapirs in subduction zones. Nat. Geosci. 5, 862–867. https://doi.org/10.1038/ngeo1634

Meyer, M., John, T., Brandt, S., Klemd, R., 2011. Trace element composition of rutile and the application of Zr-in-rutile thermometry to UHT metamorphism (Epupa Complex, NW Namibia). Lithos 126, 388–401. https://doi.org/10.1016/j.lithos.2011.07.013

1049 Meyer, M., Klemd, R., John, T., Gao, J., Menneken, M., 2016. An (in-)coherent
1050 metamorphic evolution of high-P eclogites and their host rocks in the Chinese
1051 southwest Tianshan? J. Metamorph. Geol. 34, 121–146.
1052 https://doi.org/10.1111/jmg.12175
1053 Morimoto, N., 1988. Nomenclature of Pyroxenes. Mineral. Petrol. 39, 55–76.
1054 https://doi.org/10.1007/BF01226262
1055 Nakamura, D., 2009. A new formulation of garnet–clinopyroxene geothermometer based on
1056 accumulation and statistical analysis of a large experimental data set. J. Metamorph.
1057 Geol. 27, 495–508. https://doi.org/10.1111/j.1525-1314.2009.00828.x
1058 Polino, R., 1990. Tectonic erosion at the Adria margin and accretionary processes for the
1059 Cretaceous orogeny of the Alps. Mémoire la Soc. géologique Fr. 156, 345–367.
1060 Raimbourg, H., Jolivet, L., Leroy, Y., 2007. Consequences of progressive eclogitisation on
1061 crustal exhumation, a mechanical study. Geophys. J. Int. 168, 379–401.
1062 https://doi.org/10.1111/j.1365-246X.2006.03130.x
1063 Ranero, C.R., Grevemeyer, I., Sahling, H., Barckhausen, U., Hensen, C., Wallmann, K.,
1064 Weinrebe, W., Vannucchi, P., Von Huene, R., McIntosh, K., 2008. Hydrogeological
1065 system of erosional convergent margins and its influence on tectonics and interplate
1066 seismogenesis. Geochemistry, Geophys. Geosystems 9.
1067 https://doi.org/10.1029/2007GC001679
1068 Ravna, E.J.K., 2000. The garnet – clinopyroxene Fe 2 + – Mg geothermometer : an updated
1069 calibration. J. Metamorph. Geol. 211–219.
1070 Ravna, E.J.K., Terry, M.P., 2004. Geothermobarometry of UHP and HP eclogites and
1071 schists - An evaluation of equilibria among garnet-clinopyroxene-kyanite-phengite-
1072 coesite/quartz. J. Metamorph. Geol. 22, 579–592. https://doi.org/10.1111/j.1525-
1073 1314.2004.00534.x

Remitti, F., Vannucchi, P., Bettelli, G., Fantoni, L., Panini, F., Vescovi, P., 2011. Tectonic and sedimentary evolution of the frontal part of an ancient subduction complex at the transition from accretion to erosion: The case of the Ligurian wedge of the Northern Apennines, Italy. Bull. Geol. Soc. Am. 123, 51–70. https://doi.org/10.1130/B30065.1

Richter, B., Stünitz, H., Heilbronner, R., 2016. Stresses and pressures at the quartz-to-coesite phase transformation in shear deformation experiments. J. Geophys. Res. Earth 121, 8015–8033.

Robinson, P.T., Brem, G.F., Mckee, E.H., Survey, U.S.G., Road, M., Park, M., Butte, B., 1984. Geology John Day Formation of Oregon : A distal record of early Cascade volcanism John Day Formation of Oregon : A distal record of early Cascade volcanism. Geology 12, 229–232. https://doi.org/10.1130/0091-7613(1984)12<229

Roda, M., Spalla, M.I., Marotta, A.M., 2012. Integration of natural data within a numerical model of ablative subduction: a possible interpretation for the Alpine dynamics of the Austroalpine crust. J. Metamorph. Geol. 30, 973–996.

Rowe, C.D., Moore, J.C., Remitti, F., 2013. The thickness of subduction plate boundary faults from the seafloor into the seismogenic zone. Geology 41, 991–994. https://doi.org/10.1130/G34556.1

Scheltens, M., Zhang, L., Xiao, W., Zhang, J., 2015. Northward subduction-related orogenesis of the southern Altaids: Constraints from structural and metamorphic analysis of the HP/UHP accretionary complex in Chinese southwestern Tianshan, NW China. Geosci. Front. 6, 191–209. https://doi.org/10.1016/j.gsf.2014.08.002

Scholl, D.W., von Huene, R., Vallier, T.L., Howell, D.G., 1980. Sedimentary masses and concepts about tectonic processes at underthrust ocean margins (subduction). Geology 8, 564–568. https://doi.org/10.1130/0091-7613(1980)8<564:SMACAT>2.0.CO

Scudder, R.P., Murray, R.W., Plank, T., 2009. Dispersed ash in deeply buried sediment from

1099 the northwest Pacific Ocean: An example from the Izu-Bonin arc (ODP Site 1149).
1100 Earth Planet. Sci. Lett. 284, 639–648. https://doi.org/10.1016/j.epsl.2009.05.037
1101 Smith, D.C., 1984. Coesite in clinopyroxene in the Caledonides and its implications for
1102 geodynamics. Nature 310, 641–644. https://doi.org/10.1038/310641a0
1103 Soldner, J., Oliot, E., Schulmann, K., Štípská, P., Kusbach, V., Anczkiewicz, R., 2017.
1104 Metamorphic P–T–t–d evolution of (U)HP metabasites from the South Tianshan
1105 accretionary complex (NW China) — Implications for rock deformation during
1106 exhumation in a subduction channel. Gondwana Res. 47, 161–187.
1107 https://doi.org/10.1016/j.gr.2016.07.007
1108 Syracuse, E.M., van Keken, P.E., Abers, G.A., Suetsugu, D., Bina, C., Inoue, T., Wiens, D.,
1109 Jellinek, M., 2010. The global range of subduction zone thermal models. Phys. Earth
1110 Planet. Inter. 183, 73–90. https://doi.org/10.1016/j.pepi.2010.02.004
1111 Tan, Z., Agard, P., Gao, J., John, T., Li, J.L., Jiang, T., Bayet, L., Wang, X.S., Zhang, X.,
1112 2017. P–T–time-isotopic evolution of coesite-bearing eclogites: Implications for
1113 exhumation processes in SW Tianshan. Lithos 278–281, 1–25.
1114 https://doi.org/10.1016/j.lithos.2017.01.010
1115 Tian, Z.L., Wei, C.J., 2014. Coexistence of garnet blueschist and eclogite in South Tianshan,
1116 NW China: Dependence of P-T evolution and bulk-rock composition. J. Metamorph.
1117 Geol. 32, 743–764. https://doi.org/10.1111/jmg.12089
1118 Tian, Z.L., Wei, C.J., 2013. Metamorphism of ultrahigh-pressure eclogites from the
1119 Kebuerte Valley, South Tianshan, NW China: phase equilibria and P-T path. J.
1120 Metamorph. Geol. 31, 281–300.
1121 Van der Molen, I., Van Roermund, H.L.M., 1986. The pressure path of solid inclusions in
1122 minerals: the retention of coesite inclusions during uplift. Lithos 19, 317–324.
1123 https://doi.org/10.1016/0024-4937(86)90030-7

van der Straaten, F., Halama, R., John, T., Schenk, V., Hauff, F., Andersen, N., 2012. Tracing the effects of high-pressure metasomatic fluids and seawater alteration in blueschist-facies overprinted eclogites: Implications for subduction channel processes. Chem. Geol. 292–293, 69–87.

van der Straaten, F., Schenk, V., John, T., Gao, J., 2008. Blueschist-facies rehydration of eclogites (Tian Shan, NW-China): Implications for fluid-rock interaction in the subduction channel. Chem. Geol. 255, 195–219.

Volkova, N.I., Budanov, V.I., 1999. Geochemical discrimination of metabasalt rocks of the Fan-Karategin transitional blueschist/greenschist belt, South Tianshan, Tajikistan: seamount volcanism and accretionary tectonics. Lithos 47, 201–216.

von Huene, R., Ranero, C.R., Vannucchi, P., 2004. Generic model of subduction erosion. Geology 32, 913–916. https://doi.org/10.1130/G20563.1

Wada, I., Wang, K., 2009. Common depth of slab-mantle decoupling: Reconciling diversity and uniformity of subduction zones. Geochemistry, Geophys. Geosystems 10. https://doi.org/10.1029/2009GC002570

Wakabayashi, J., 2015. Anatomy of a subduction complex: Architecture of the Franciscan Complex, California, at multiple length and time scales. Int. Geol. Rev. 57, 669–746. https://doi.org/10.1080/00206814.2014.998728

Wang, B., Shu, L., Faure, M., Jahn, B. ming, Cluzel, D., Charvet, J., Chung, S. lin, Meffre, S., 2011. Paleozoic tectonics of the southern Chinese Tianshan: Insights from structural, chronological and geochemical studies of the Heiyingshan ophiolitic mélange (NW China). Tectonophysics 497, 85–104. https://doi.org/10.1016/j.tecto.2010.11.004

Waters, D.J., Martin, H.N., 1996. The garnet-cpx-phengite barometer—recommended calibration and calculation method. URL http//www. earth. ox. ac. uk/~

1149 davewa/research/eclogites/ecbarcal. html accessed 3, 14.
1150 Wei, C., Wang, W., Clarke, G.L., Zhang, L., Song, S., 2009. Metamorphism of
1151 High/ultrahigh-pressure Pelitic–Felsic Schist in the South Tianshan Orogen, NW
1152 China: Phase Equilibria and P–T Path. J. Petrol. 50, 1973–1991.
1153 Wei, C.J., Powell, R., Zhang, L.F., 2003. Eclogites from the south Tianshan, NW China:
1154 petrological characteristic and calculated mineral equilibria in the Na2O–CaO–FeO–
1155 MgO–Al2O3–SiO2–H2O system. J. Metamorph. Geol. 21, 163–179.
1156 Whitney, D.L., Evans, B.W., 2010. Abbreviations for names of rock-forming minerals. Am.
1157 Mineral. 95, 185–187. https://doi.org/10.2138/am.2010.3371
1158 Xiao, W., Santosh, M., 2014. The western Central Asian Orogenic Belt: A window to
1159 accretionary orogenesis and continental growth. Gondwana Res. 25, 1429–1444.
1160 https://doi.org/10.1016/j.gr.2014.01.008
1161 Xiao, W.J., Windley, B.F., Huang, B.C., Han, C.M., Yuan, C., Chen, H.L., Sun, M., Sun, S.,
1162 Li, J.L., 2009. End-Permian to mid-Triassic termination of the accretionary processes
1163 of the southern Altaids: implications for the geodynamic evolution, Phanerozoic
1164 continental growth, and metallogeny of Central Asia. Int. J. Earth Sci. 98, 1189–1217.
1165 Yamato, P., Agard, P., Burov, E., Le Pourhiet, L., Jolivet, L., Tiberi, C., 2007. Burial and
1166 exhumation in a subduction wedge: Mutual constraints from thermomechanical
1167 modeling and natural P-T-t data (Schistes Lustrés, western Alps). J. Geophys. Res.
1168 Solid Earth 112, 1–28. https://doi.org/10.1029/2006JB004441
1169 Zack, T., Moraes, R., Kronz, A., 2004. Temperature dependence of Zr in rutile: Empirical
1170 calibration of a rutile thermometer. Contrib. to Mineral. Petrol. 148, 471–488.
1171 https://doi.org/10.1007/s00410-004-0617-8
1172

Figure captions

Figure 1: **(a)** Pressure-temperature (P-T) diagram with an estimated P-T-time path for the rocks of the Tianshan Akeyazi metamorphic complex (AMC), the grey arrow represents the estimated P-T trajectory from THERMOCALC averagePT, modified after Tan et al. (2017); peak P-T conditions estimated in this study are reported on the figure (red box). The curve reflecting the quartz-coesite transition and the jadeite/kyanite-paragonite transitions are after Richter et al (2016) and (Chopin et al., 1991) et al (1991) **(b)** Previous geodynamic interpretations for the AMC: 1) tectonic mélange, with mafic blocks originating from various depths in a sedimentary matrix (Model 1; bottom left; modified after Klemd et al., 2011) or sub-belt model, with a high-pressure (HP) unit versus ultra-high-pressure (UHP) unit (Model 2; bottom right; modified after Lü et al. (2009).

Figure 2: **(a)** Map of the Central Asian Orogenic Belt modified after Long et al. (2011). **(b)** Regional tectonic map of the Chinese Tianshan modified after (Gao et al., 1999). **(c)** Geological map of the Tianshan Akeyazi metamorphic complex in NW China displaying the suggested "HP/UHP shear zone" modified after Lü et al (2012). Profiles a, b and c represent localities for field views of figure 4.

Figure 3: Field photographs illustrating the diverse lithologies found in the metamorphic belt. Photographs a to d show the various main lithologies from metasedimentary (S-type, **a**), to intermediate volcano-sclastic (V-type, **b**), to pure mafic (M-type), with eclogites (ss) composed of omphacite, garnet, and quartz **(c)** and blueschist (ss) with blue amphibole and pseudomorphs after lawsonite **(d)**. Interlayering between the different rock types (S-, V-, and M-) are represented here in e to h, with the interlayering of: **e)** thin S-type layers and thicker

V-type laryers, **f)** a mafic blueschistic layer with a pelitic mica-rich layer, **g)** S-type and M-type eclogitic layers (omphacite, garnet and glaucophane layers), **h)** V-type layers with varying mafic and pelitic mineral components and a thick mafic rocks layer. **(i)** Large-scale deformation of volcanoclastic rocks, with the thin and finely schistosed more pelitic layers and thicker more mafic layers. **(j)** Shearing of a volcanoclastic rock with fish structure of amphibole-rich and quartz-rich components. **(k)** Volcanoclastic rock with an intermediate composition, in which deformation is accommodated by a white mica and amphibole schistosity and shearing displayed by quartz fish structures and rotated garnets, with asymmetric strain shadows around garnet that indicate shearing **(l)** Greenschist-facies metasedimentary rock from the northern part of the metamorphic belt, composed of chlorite, albite, green amphibole, and lacking minerals indicating high-pressure. **(m)** Unmetamorphosed micro-conglomerate likely representing the detrital filling of a small sedimentary basin overlying the greenschist/high-pressure-detachment (GHPD) of the Muzetekexie valley (see Fig. 4a). **(n)** Meter-thick carbonate layers intercalated between volcano-clastic layers. **(o)** Glaucophanite composed of white mica and ankerite in a glaucophane matrix (note the presence of an omphacite-quartz vein to the left). **(p)** Former pillow basalt, showing a contrast in chemical equilibration and/or composition between core (blueschist) and rim (eclogite). **(q)** Blueschistic pillow breccias filled with carbonates, located in the southeastern part of Akesayi. All mineral abbreviations after Whitney and Evans (2010).

Figure 4: Field data synthesis of lithology. **(a)** Lithological map corresponding with data points (circles); volcanoclastic rocks are divided in three groups, according to their mafic and pelitic proportion, from mica-rich (light grey) to mafic (black) with intermediate composition (dark grey); note that some of the carbonates form continuous large mapable

bodies. **(b)** Synthetic and schematic lithological profile from north (top) to south (bottom): 1) volcanics of the Yili-Junggar plates, 2) northern folded greenschist-unit, overlain by a small unmetamorphosed sedimentary basin 3) HP-UHP unit composed of: 3a) a thick metavolcano-clastic sequence showing a gradient from pelitic to mafic, with occasional carbonate intercalations, 3b) pillow basalts and breccias under blueschist- and eclogite-facies conditions. The continuity of the pillow basalts further south is unknown (green gradient in 5a). The different sub-units of the HP-UHP unit are reported on the sections.

Figure 5: Field views of **(a)** the Muzetekexie valley and **(b)** the south-west and **(c)** central-eastern parts of the Akesayi valley. **(a)** Large detachment fault with an area of ~ 50 m of deformation – namely the greenschist/high-pressure-detachment (GHPD) – between the HP-UHP unit in the south and the greenschist-unit in the north (red line), the dotted part of the line represents a more diffuse nature of this contact, a local unmetamorphosed basin is unconformably overlying the greenschist-unit. **(b), (c)** Clear E-W striking, north dipping schistosity (black), and km-scale shear zones (red planes). **(b)** Smaller shear zones with different orientation are observed in addition to the km-scale shear zone. **(c)** Pluridecametric fold near the shear zone.

Figure 6: Field data synthesis of structures. **(a)** Simplified structural map of the studied area showing a ca. E-W striking north dipping schistosity (black), shearing (red lines) with a top-to-the-north sense of shearing as indicated by blueschist- (blue arrows) and greenschist-facies lineation (green arrows), separating structural sub-units (labelled 1 to 5). **(b)** Stereoplot showing poles, contours, and average measurements (gray area) of the schistosity (D_n to D_{n+1} deformation stage), i.e. with an E-W strike and dipping north (left); stereoplots

are equiareal lower hemisphere projection. **(c)** Mean shear plane (C, red line, D_{n+2} deformation stage) determined after measurements average (red area). **(d)** Rose diagram with the cluster of lineation values around a N-S orientation with top-to-the-north shear senses (D_{n+2} to D_{n+3} deformation stage). N represents the number of measurements. **(e)** Schematic illustration of the shearing (D_{n+2}) affecting both S(D_n) and Sc(D_{n+1}), with typical S/C structures. **(f)** Synthetic N-S cross section highlighting a lithological gradient from more mafic in the South to more pelitic in the North, the presence of strongly deformed sedimentary horizons and pervasive deformation. Modified after Bayet et al. (2018). Labels 1 to 5 correspond to the different units reported on the map (a). Note that this cross-section is a synthesis of deformation observed from North to South through the entire studied area and does not represent a specific cross-section. **(g)** Three-dimension sketch of the different deformation stages observed in the field, illustrating the crosscutting relations between each other. Note the difference of deformation between the less (S-type) and more (M-type) competent rocks.

Figure 7: Photographs of the different deformation features at cm to m scale. **(a,b)** Shear band in a volcano-clastic rock depicting mylonitisation in its center with decreasing deformation outwards. **(c,d)** Mafic boudin wrapped in metasedimentary layers, displaying schistosity (S, black), shearing (C, red), and folding of the schistosity in the volcano-clastic rock (bottom); quartz veins are present. A zoom of the deformation displays nice S/C structures at the cm-scale. **(e,f)** Crenulation schistosity (Sc, orange) overprinting the previous schistosity Sn in a volcano-clastic rock. **(g)** Metasedimentary rock presenting shearing (C) affecting the main schistosity (Sn ± Sn+1) at blueschist-facies conditions, as indicated by ubiquitous glaucophane lineation **(j)**. Normal **(h)** and disharmonic **(i**; red dotted lines**)** folds in volcano-clastic rocks (blueschist- to eclogite-metamorphism). **(k,l)**

1271 Development of C' structures, oblique to C, with pervasive schistosity in a metasedimentary
1272 rock overprinted by greenschist-facies metamorphism. Greenschist-facies deformation, with
1273 the presence of chlorite, is visible in the zoomed part.
1274

1275 Figure 8: Photographs of typical microstructures: **(a)** eclogite-facies M-type rock showing
1276 little to no deformation (when 'purely' mafic), plane polarised light. **(b)**, **(c)** V-type rocks
1277 with increasing deformation displayed by schistosity related to increase of the white mica
1278 content; plane polarised light**. (d)** Blueschist-facies deformation characterized by white mica
1279 (re)crystallization; plane polarised light. **(e)** S-type rock presenting a pervasive schistosity
1280 (S, black lines), with quartz inclusion in a garnet host, displaying a former schistosity (S_{n-1},
1281 red lines); crossed polars. **(g)** Crenulation schistosity (S_C, red dashed lines) in a V- type
1282 rock; crossed (top) and plane polariser light with cartoon (bottom). **(h)** Shearing in a garnet-
1283 bearing S-type rock, represented by the development of asymmetric quartz shadows around
1284 garnets porphyroblasts and pervasive white micas schistosity; plane polarised light (top) and
1285 systematic cartoon, (bottom). Mineral abbreviations after Whitney and Evans (2010).
1286

1287 Figure 9: Backscattered electron (BSE) images: **(a)** greenschist-facies metasedimentary rock
1288 (from the greenschist-unit), with a paragenesis of Ab-Ep-Chl-Act. **(b)** Blueschist-facies
1289 mafic to vocano-clastic rock composed of a glaucophane-phengite-paragonite matrix with
1290 quartz nd garnet porphyroblasts. **(c)** Eclogite-facies mafic rock, with a clinopyroxene matrix
1291 and euhedral phenocrysts of epidote, glaucophane, quartz and phengite. **(d)** Eclogite-facies
1292 mafic rock with euhedral garnets hosting numerous inclusions, in a clinopyroxene matrix
1293 with euhedral epidote, phengite, glaucophane, and additional ankerite. Variation in grey
1294 scale of the clinoproxenes is due to a heterogeneities in composition (see text more for
1295 details) **(e)** Vocanoclastic rock showing blueschist-facies retrogression typically indicated by

1296 the association of blue-green amphibole (barroisite) and small garnets in an albite matrix.
1297 Darker minerals close to the amphibole are calcite. **(f)** Greenschist-facies retrogression in a
1298 metasedimentary rock indicated by chloritisation of garnets, and numerous chlorite patches.
1299 Mineral abbreviations after Whitney and Evans (2010).

1300

1301 Figure 10: Chemical composition of garnet, phengite, amphibole, and clinopyroxene
1302 (electron microprobe data). **(a)** Garnet ternary diagrams presenting a high almandine
1303 component. Eclogite samples (green field) present a higher grossular (Ca) component while
1304 blueschist samples (blue field) are closer to the almandine (Fe) end-member (left).
1305 Micaschists (yellow field) present more variability, however, with a tendency towards higher
1306 pyrope (Mg) content (right), variation in garnet composition is likely due to variation in the
1307 bulk composition; **(b)** Phengite composition in the Fe+Mg vs Si p.f.u. diagram, the 1:1 black
1308 line represents the tschermak substitution; **(c)** Composition of clinopyroxene in a ternary Di-
1309 Hd/Jd/Ae diagram after Morimoto (1988). Most clinopyroxenes fall into the omphacite field,
1310 with few outlier compositions in the Aeg-Aug field. Different colors refer to pyroxene
1311 inclusions (orange field) and matrix pyroxene (blue field). Abbreviations after Whitney and
1312 Evans (2010); **(d)** Composition of amphibole, classified as glaucophane (blue field),
1313 barroisite, magnesio-hornblende, winchite or richterite and actinolite after Leake et al.,
1314 (1997, 2004). Blue amphibole is mostly glaucophane (blue area). **e)** Sample names and
1315 symbols legend: yellow symbols refer to S- to V-types rocks, blue symbols to blueschist-
1316 facies V- to M- type rocks, and dark green symbols to eclogite-facies V- to M- type rocks.
1317

1318 Figure 11: Illustration of estimated peak P-T conditions. **(a)** Histogram of average T_C
1319 (obtained with Raman spectroscopy of carbonaceous material; red) and T_{Zr} (obtained with

Zr in rutile; orange) for all samples, with an average value of ca. 538 °C. **(b)** Distribution map of averaged estimated peak temperatures (T_C, red numbers and T_{Zr}, orange numbers), with an average temperature of ca. 535 °C.**(c)** Comparison of peak temperatures for the individual lithologies, from the metasedimentary (bottom) to mafic (top), with blue indicating dominantly blueschist mineral assemblages and green eclogite mineral assemblages. **(d)** Coesite Raman spectra of all coesite samples reported in this study. **(e)** Distribution map of averaged estimated peak pressure inferred from coesite (≥ 2.6 GPa) and estimated via the QuiG and phengite barometry (black numbers; see text for details). Coesite findings from this and other studies are reported as stars on each map.

Figure 12: Schematic geodynamic evolution model of the Tianshan Akeyazi metamorphic complex. **(a)** Volcanoclastic inputs; scrapping off pieces from the accretionary prism and deposition of volcano-clastic material in the trench, further dragged down the subduction zone. **(b)** Burial, detachment and stacking at greenschist- and UHP- conditions; the UHP sequence consists of the successive accretion of several slices – separated by thrusts contacts – of material dragged down on top of the oceanic plate. Numbers 1 to 4 correpond to the different sub-units observed in the field in the volcano-clastic part of the UHP unit. **(c)** Exhumation and dismembering of the HP-UHP unit at blueschist conditions, with reactivation of the previous thrusts as blueschist-facies shear zones. Parts of the oceanic plate (pillow basalts) are scrapped of prior or during the exhumation, forming the last sub-unit of the UHP sequence (number 5). **(d)** Present day configuration: pervasive deformation and detachment between the greenschist-unit and the HP-UHP sequence (Modified after Bayet et al. (2018)). Peak temperature estimates reported above the transect, according to their distance from the Greenschist / high-pressure detachment (GHPD), show a great homogeneity. Peak pressure estimates reported under the transect, according to their position

in the different sub-units, show that no major gap in pressure exists between the sub-units.

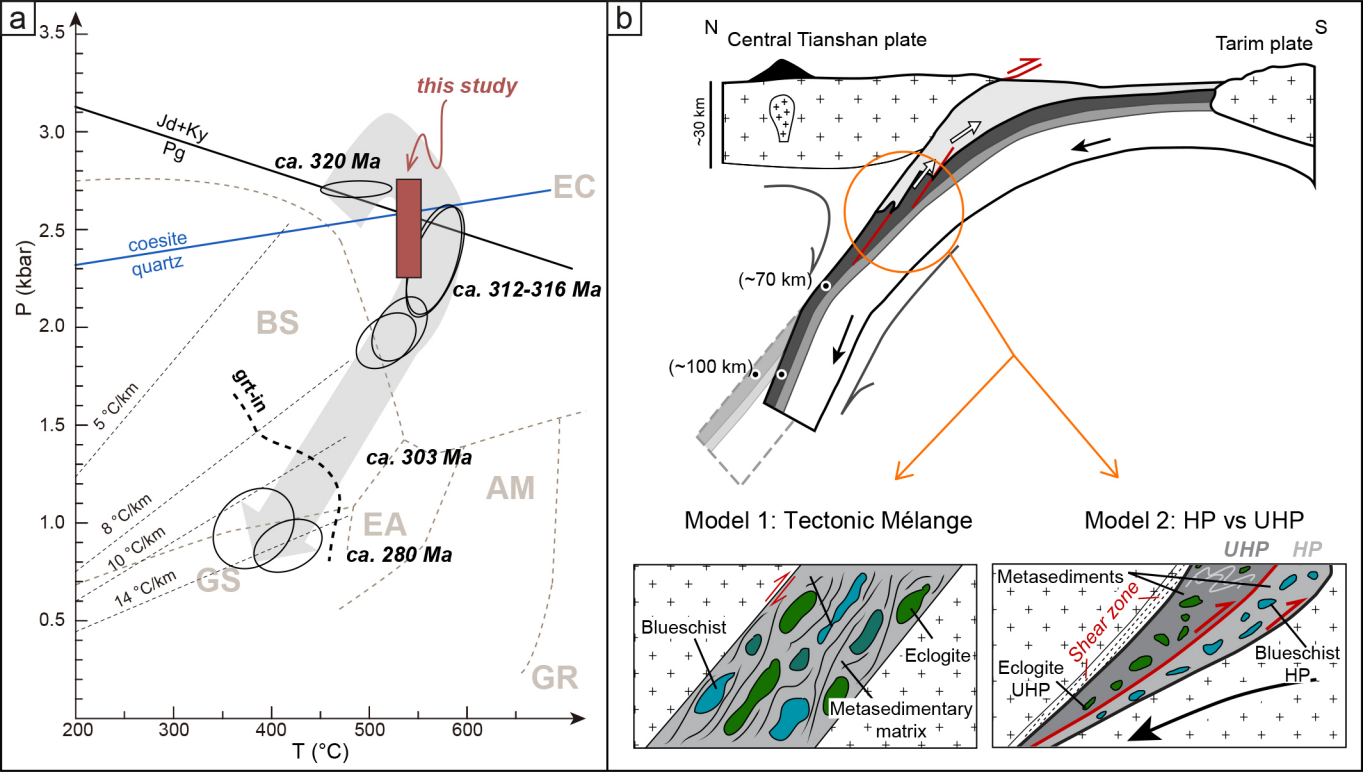
a
b
this study
Jd+Ky
Pg
ca. 320 Ma
EC
coesite
quartz
ca. 312-316 Ma
BS
grt-in
5 °C/km
8 °C/km
10 °C/km
14 °C/km
ca. 303 Ma
AM
EA
ca. 280 Ma
GS
GR
P (kbar)
T (°C)
N
Central Tianshan plate
Tarim plate
S
~30 km
(~70 km)
(~100 km)
Model 1: Tectonic Mélange
Model 2: HP vs UHP
Blueschist
Eclogite
Metasedimentary
matrix
UHP
HP
Metasediments
Shear zone
Eclogite
UHP
Blueschist
HP

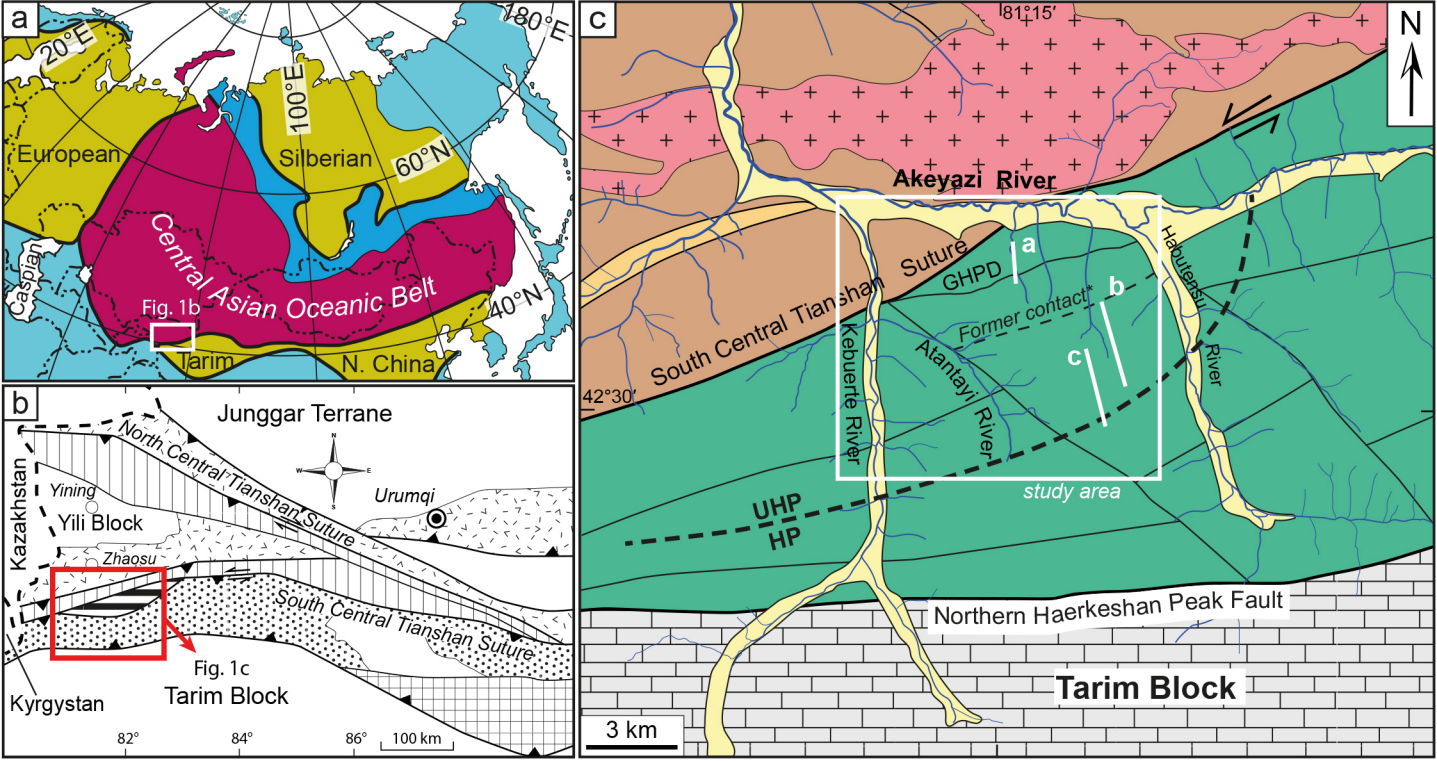
a
20°E
100°E
180°E
60°N
40°N
European
Siberian
Caspian
Central Asian Oceanic Belt
Fig. 1b
Tarim
N. China
b
Junggar Terrane
North Central Tianshan Suture
Kazakhstan
Yining
Yili Block
Urumqi
Zhaosu
South Central Tianshan Suture
Fig. 1c
Tarim Block
Kyrgystan
82°
84°
86°
100 km
c
81°15′
N
Akeyazi River
Suture
GHPD
a
Former contact*
b
c
Kebuerte River
Atantayi River
Habulengsu River
42°30′
South Central Tianshan
study area
UHP
HP
Northern Haerkeshan Peak Fault
Tarim Block
3 km
Late Paleozoic volcanic and volcanoclastic rocks
Metabasic association
Precambrian basement, Paleozoic granites and strata
Paleozoic sedimentary rocks
Precambrian basement
Meso-Cenozoic cover
Trust
Fault
Strike-Slip fault
Provincial capital
City
Calc-alkaline granite
Silurian volcanic clastic rock
Limestone and marble
Metamorphic belt
Marble, limestone and dolomite
Alluvium

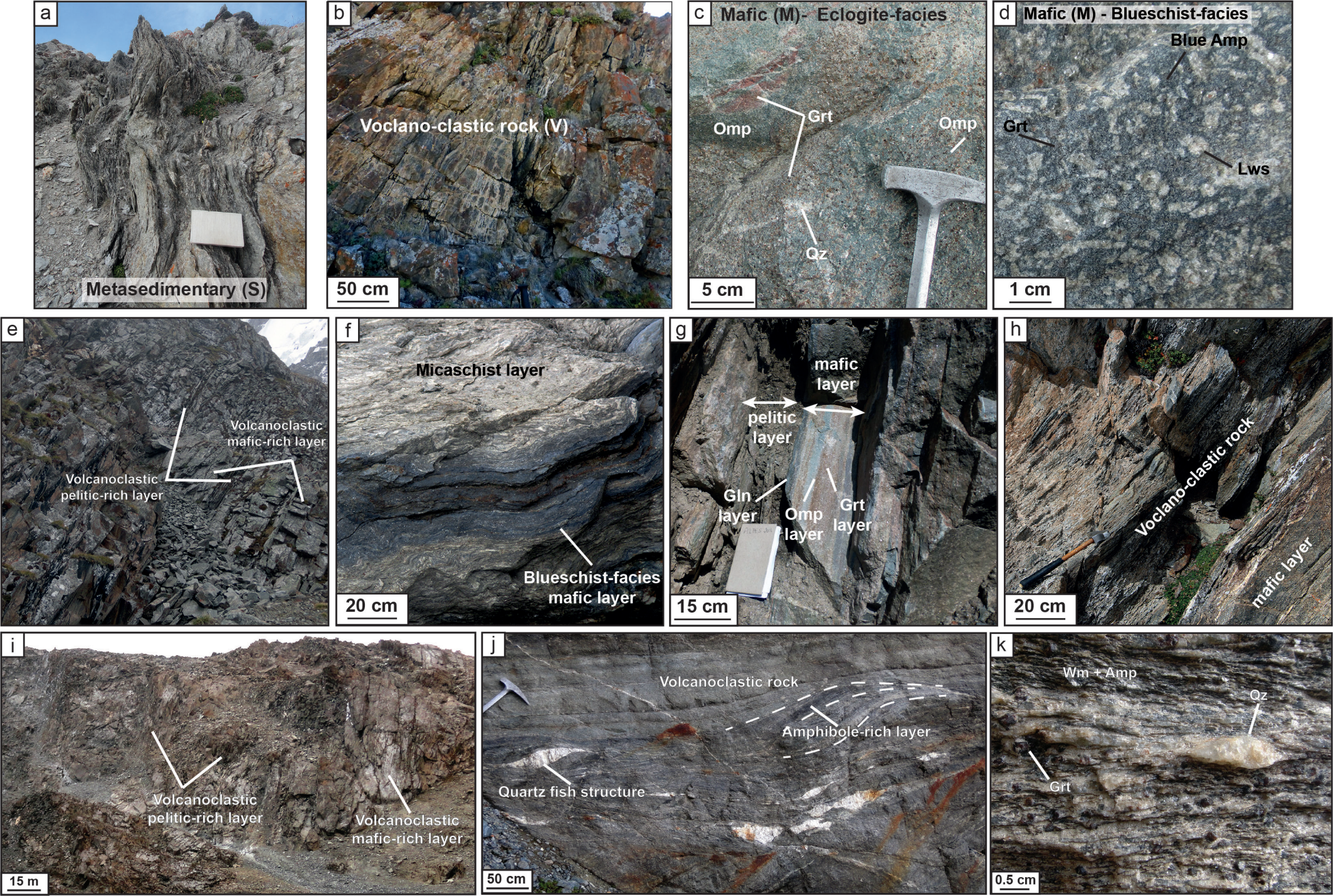
a
Metasedimentary (S)
b
Voclano-clastic rock (V)
50 cm
c
Mafic (M)- Eclogite-facies
Omp
Grt
Omp
Qz
5 cm
d
Mafic (M) - Blueschist-facies
Blue Amp
Grt
Lws
1 cm
e
Volcanoclastic mafic-rich layer
Volcanoclastic pelitic-rich layer
f
Micaschist layer
Blueschist-facies mafic layer
20 cm
g
mafic layer
pelitic layer
Gln layer
Omp layer
Grt layer
15 cm
h
Voclano-clastic rock
mafic layer
20 cm
i
Volcanoclastic pelitic-rich layer
Volcanoclastic mafic-rich layer
15 m
j
Volcanoclastic rock
Amphibole-rich layer
Quartz fish structure
50 cm
k
Wm + Amp
Qz
Grt
0.5 cm


l
Chlorite-rich Greenschist
5 cm

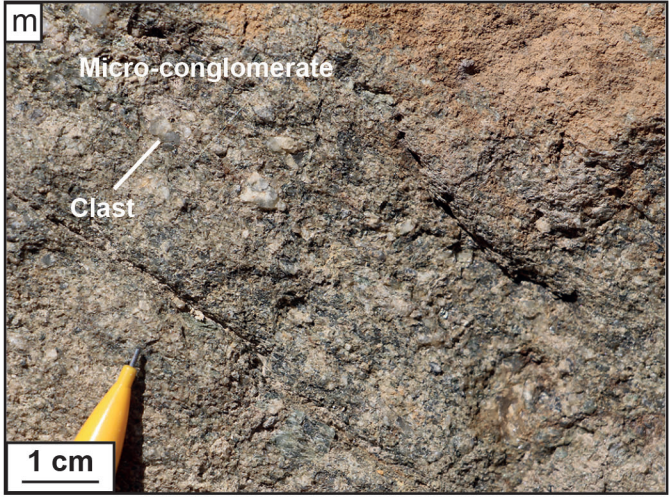
m
Micro-conglomerate
Clast
1 cm

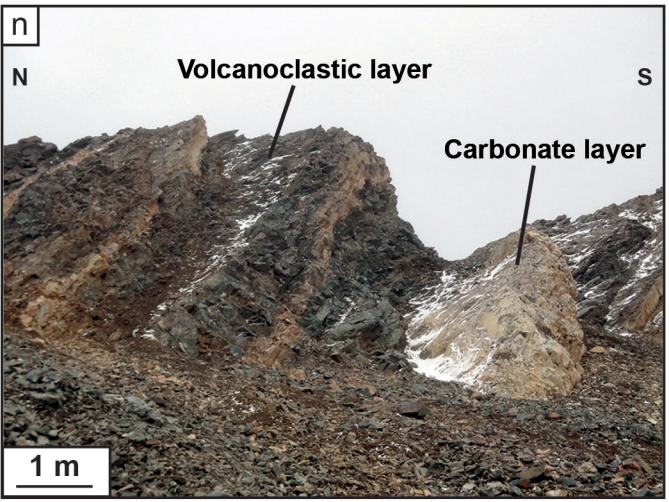
n
N
Volcanoclastic layer
S
Carbonate layer
1 m

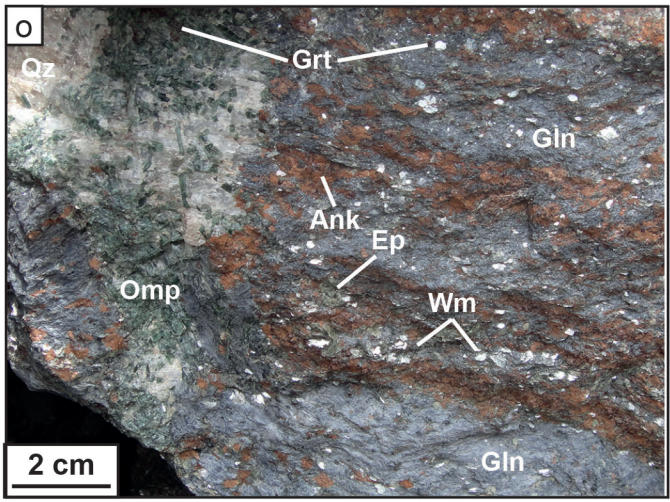
o
Qz
Grt
Gln
Ank
Ep
Omp
Wm
2 cm
Gln

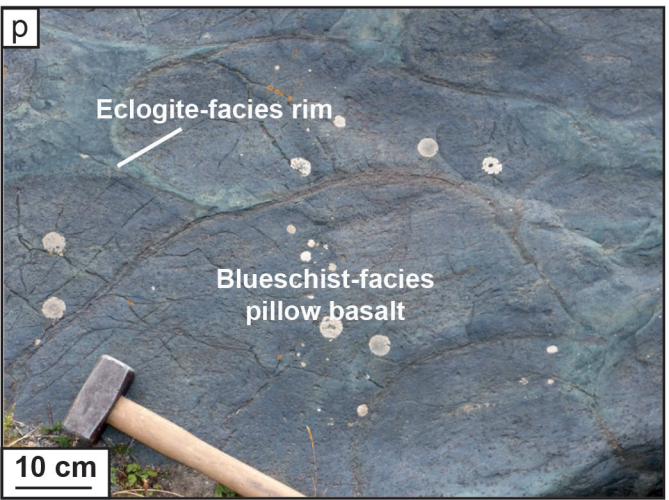
p
Eclogite-facies rim
Blueschist-facies
pillow basalt
10 cm

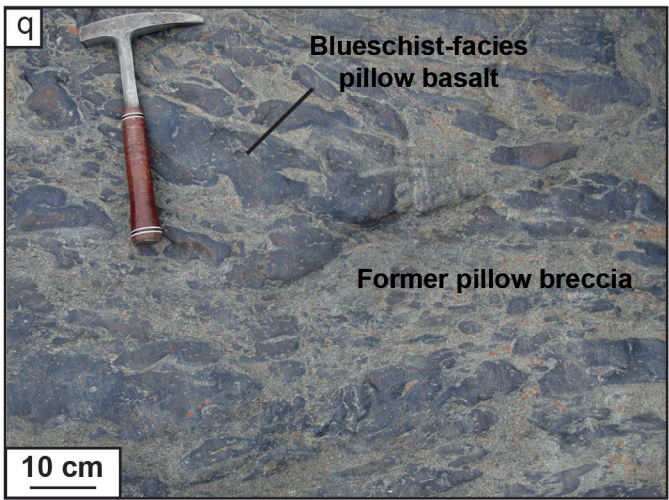
q
Blueschist-facies
pillow basalt
Former pillow breccia
10 cm

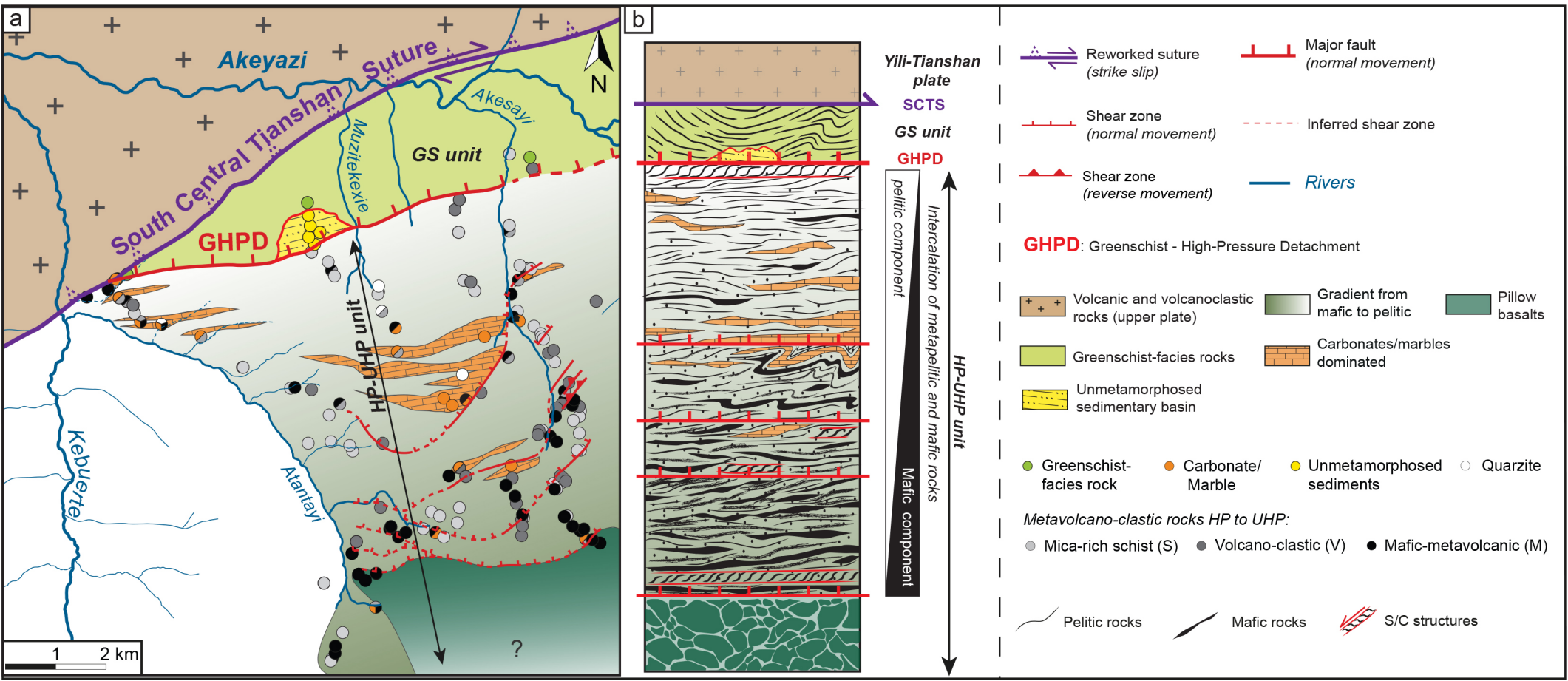
a
Akeyazi
South Central Tianshan Suture
Akesayi
Muztiekexie
GS unit
GHPD
HP-UHP unit
Kebuerte
Atantayi
?
N
1
2 km
b
Yili-Tianshan plate
SCTS
GS unit
GHPD
pelitic component
Intercalation of metapelitic and mafic rocks
Mafic component
HP-UHP unit
Reworked suture (strike slip)
Major fault (normal movement)
Shear zone (normal movement)
Inferred shear zone
Shear zone (reverse movement)
Rivers
GHPD: Greenschist - High-Pressure Detachment
Volcanic and volcanoclastic rocks (upper plate)
Gradient from mafic to pelitic
Pillow basalts
Greenschist-facies rocks
Carbonates/marbles dominated
Unmetamorphosed sedimentary basin
Greenschist-facies rock
Carbonate/ Marble
Unmetamorphosed sediments
Quarzite
Metavolcano-clastic rocks HP to UHP:
Mica-rich schist (S)
Volcano-clastic (V)
Mafic-metavolcanic (M)
Pelitic rocks
Mafic rocks
S/C structures

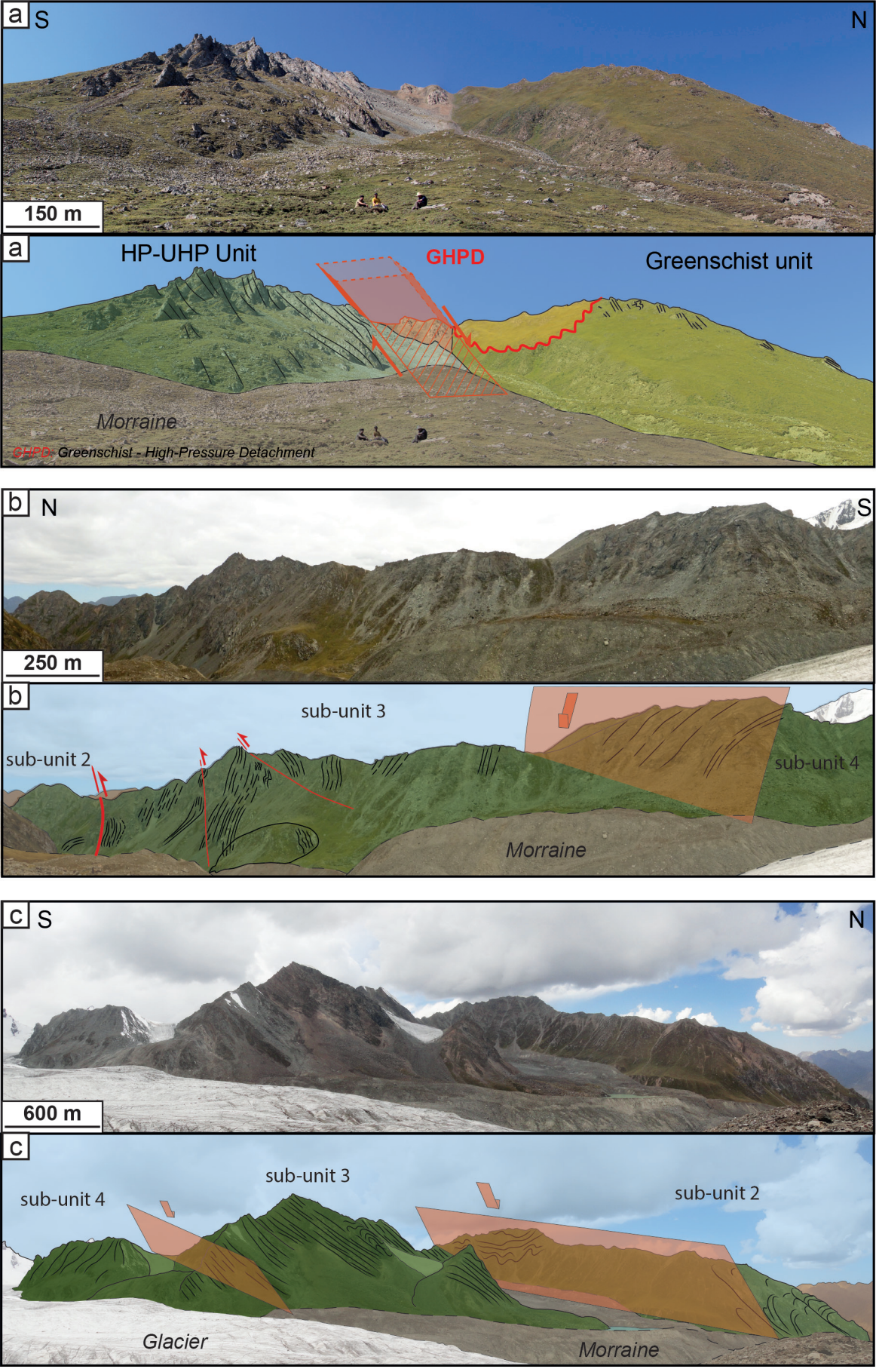
a
S
N
150 m
a
HP-UHP Unit
GHPD
Greenschist unit
Morraine
GHPD: Greenschist - High-Pressure Detachment
b
N
S
250 m
b
sub-unit 3
sub-unit 2
sub-unit 4
Morraine
c
S
N
600 m
c
sub-unit 3
sub-unit 4
sub-unit 2
Glacier
Morraine

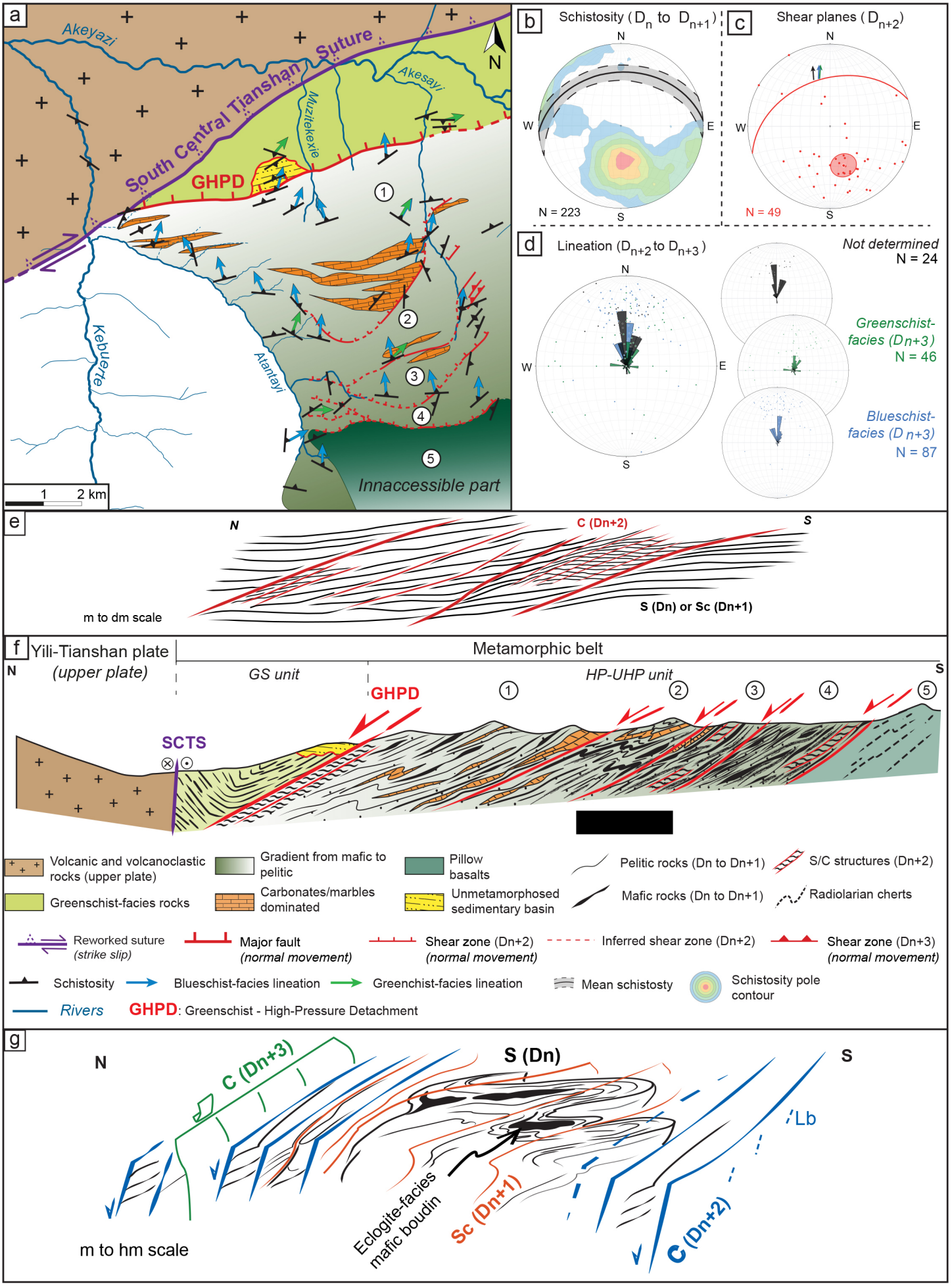
a
Akeyazi
South Central Tianshan Suture
Muzitekexie
Akesayi
GHPD
Kebuerte
Atantayi
1
2
3
4
5
Innaccessible part
1 2 km
N
b
Schistosity (D_n to D_{n+1})
N
W
E
S
N = 223
c
Shear planes (D_{n+2})
N = 49
d
Lineation (D_{n+2} to D_{n+3})
Not determined
N = 24
Greenschist-facies (D_{n+3})
N = 46
Blueschist-facies (D_{n+3})
N = 87
e
N
S
C (Dn+2)
S (Dn) or Sc (Dn+1)
m to dm scale
f
Yili-Tianshan plate
(upper plate)
Metamorphic belt
GS unit
HP-UHP unit
GHPD
SCTS
Volcanic and volcanoclastic rocks (upper plate)
Greenschist-facies rocks
Gradient from mafic to pelitic
Carbonates/marbles dominated
Pillow basalts
Unmetamorphosed sedimentary basin
Pelitic rocks (Dn to Dn+1)
Mafic rocks (Dn to Dn+1)
S/C structures (Dn+2)
Radiolarian cherts
Reworked suture (strike slip)
Major fault (normal movement)
Shear zone (Dn+2) (normal movement)
Inferred shear zone (Dn+2)
Shear zone (Dn+3) (normal movement)
Schistosity
Blueschist-facies lineation
Greenschist-facies lineation
Mean schistosty
Schistosity pole contour
Rivers
GHPD: Greenschist - High-Pressure Detachment
g
N
S
C (Dn+3)
S (Dn)
Lb
Eclogite-facies mafic boudin
Sc (Dn+1)
C (Dn+2)
m to hm scale

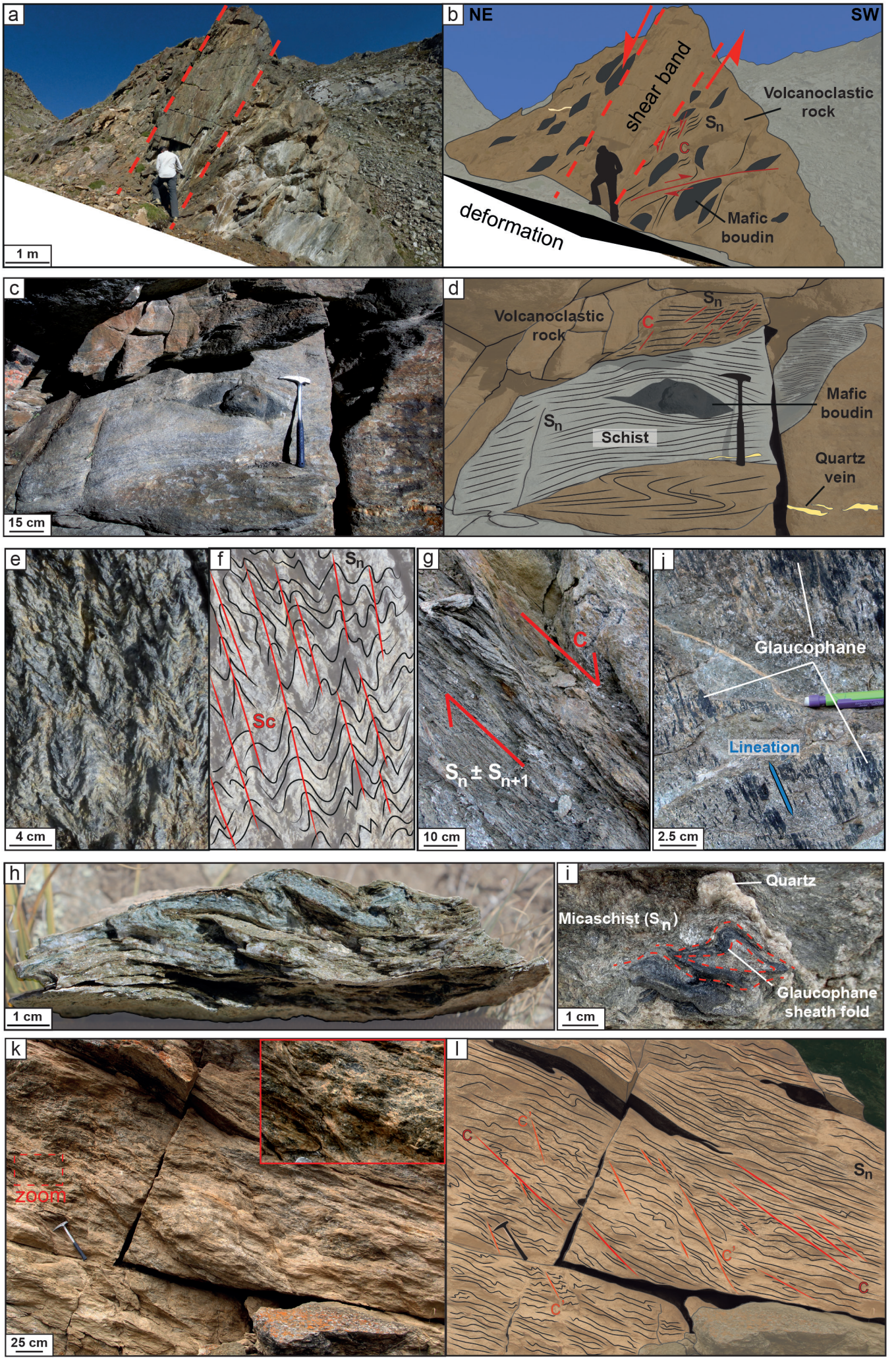
a
1 m
b
NE
SW
shear band
Volcanoclastic rock
S_n
C
deformation
Mafic boudin
c
15 cm
d
Volcanoclastic rock
S_n
C
Mafic boudin
S_n
Schist
Quartz vein
e
4 cm
f
S_n
Sc
g
C
$S_n \pm S_{n+1}$
10 cm
j
Glaucophane
Lineation
2.5 cm
h
1 cm
i
Quartz
Micaschist (S_n)
Glaucophane sheath fold
1 cm
k
zoom
25 cm
l
C
C'
S_n
C'
C'
C

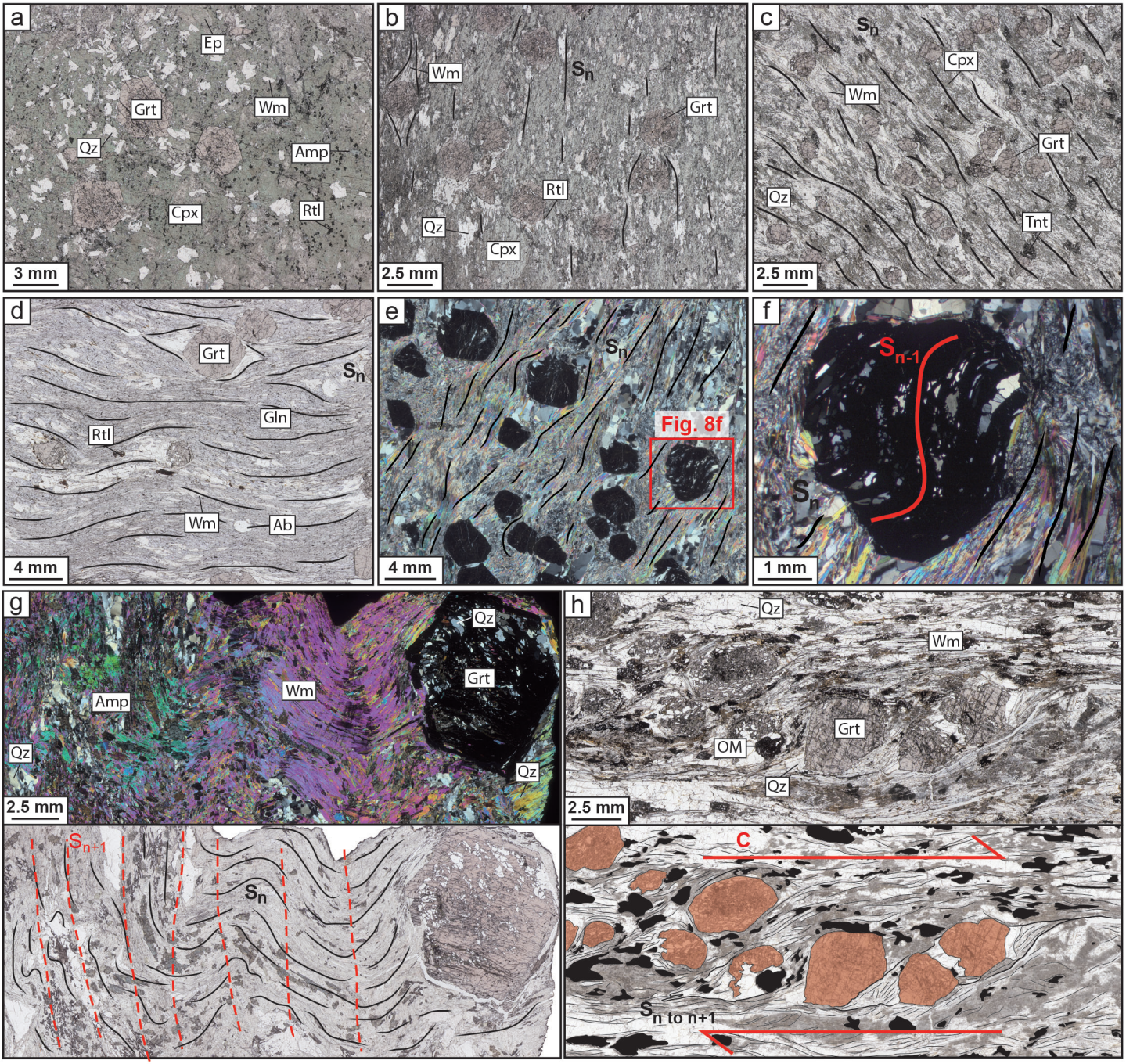
a
Ep
Grt
Wm
Qz
Amp
Cpx
Rtl
3 mm
b
Wm
Sn
Grt
Rtl
Qz
Cpx
2.5 mm
c
Sn
Cpx
Wm
Grt
Qz
Tnt
2.5 mm
d
Grt
Sn
Gln
Rtl
Wm
Ab
4 mm
e
Sn
Fig. 8f
4 mm
f
Sn-1
Sn
1 mm
g
Qz
Grt
Amp
Wm
Qz
Qz
2.5 mm
Sn+1
Sn
h
Qz
Wm
Grt
OM
Qz
2.5 mm
C
Sn to n+1

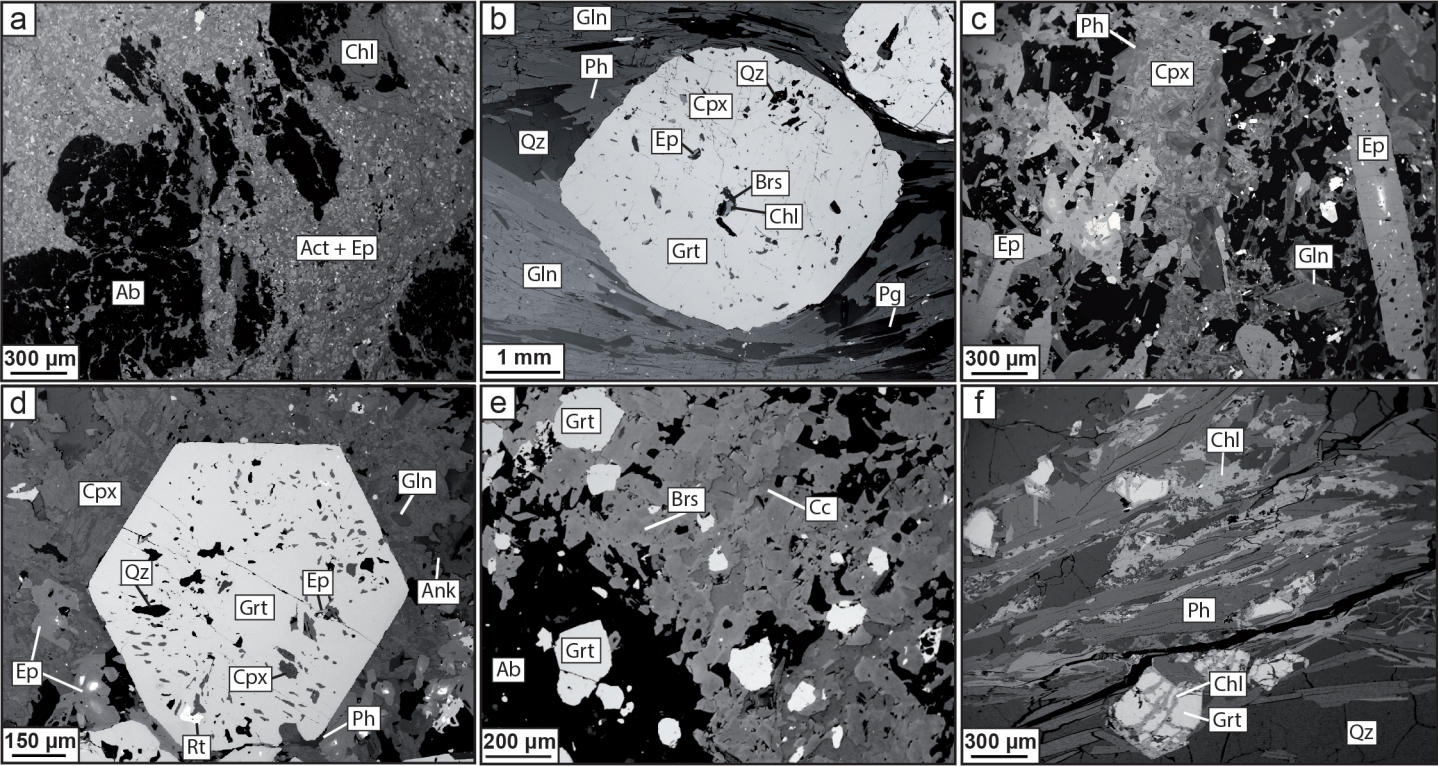
a
Chl
Act + Ep
Ab
300 µm
b
Gln
Ph
Qz
Cpx
Ep
Qz
Brs
Chl
Grt
Gln
Pg
1 mm
c
Ph
Cpx
Ep
Ep
Gln
300 µm
d
Cpx
Gln
Qz
Ep
Grt
Ank
Ep
Cpx
Ph
Rt
150 µm
e
Grt
Brs
Cc
Ab
Grt
200 µm
f
Chl
Ph
Chl
Grt
Qz
300 µm

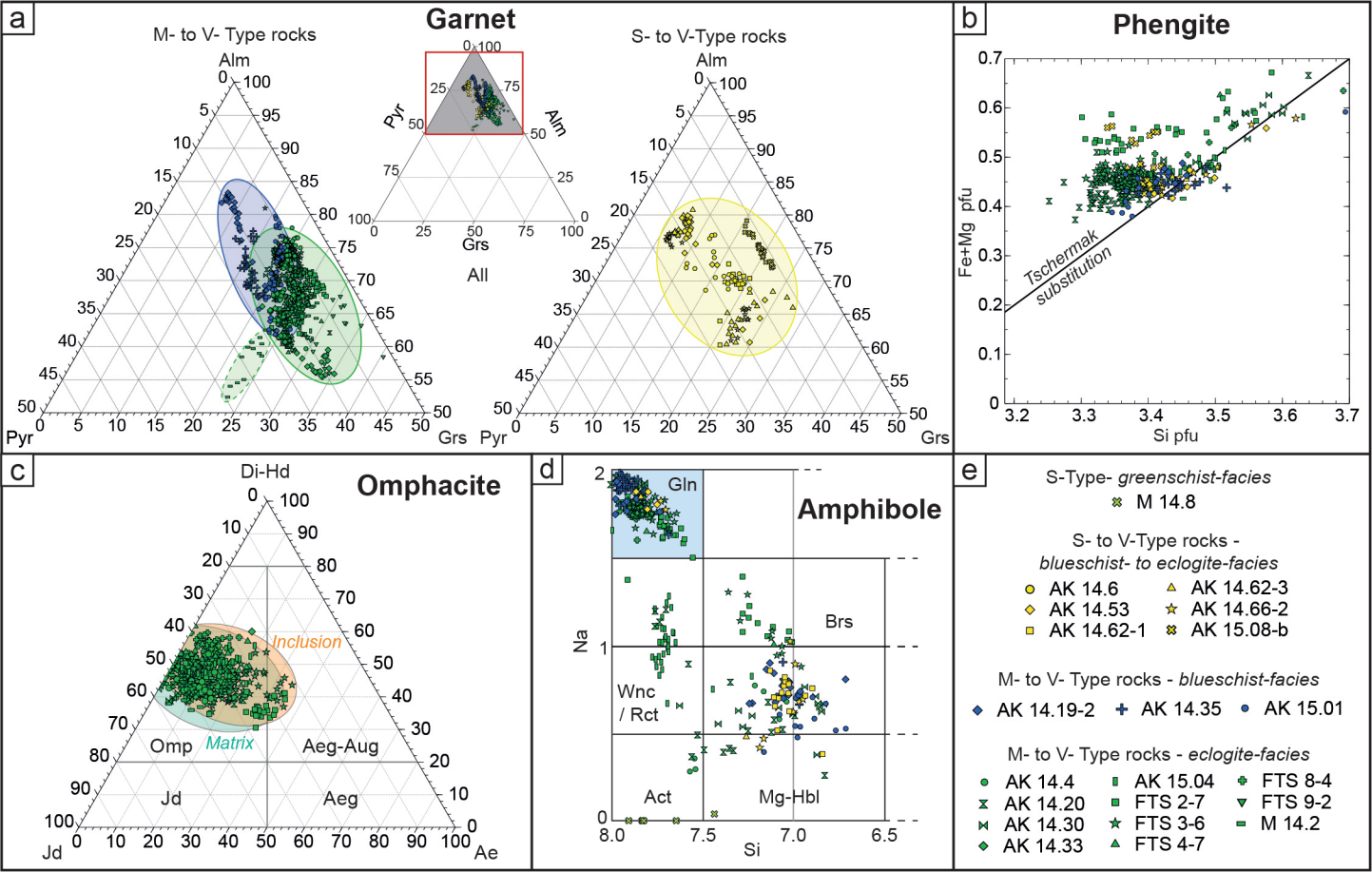
a
Garnet
M- to V- Type rocks
S- to V-Type rocks
All
Alm
Pyr
Grs
b
Phengite
Fe+Mg pfu
Si pfu
Tschermak substitution
c
Omphacite
Di-Hd
Jd
Ae
Inclusion
Matrix
Omp
Aeg-Aug
Jd
Aeg
d
Amphibole
Na
Si
Gln
Brs
Wnc / Rct
Act
Mg-Hbl
e
S-Type- greenschist-facies
M 14.8
S- to V-Type rocks - blueschist- to eclogite-facies
AK 14.6
AK 14.53
AK 14.62-1
AK 14.62-3
AK 14.66-2
AK 15.08-b
M- to V- Type rocks - blueschist-facies
AK 14.19-2
AK 14.35
AK 15.01
M- to V- Type rocks - eclogite-facies
AK 14.4
AK 14.20
AK 14.30
AK 14.33
AK 15.04
FTS 2-7
FTS 3-6
FTS 4-7
FTS 8-4
FTS 9-2
M 14.2

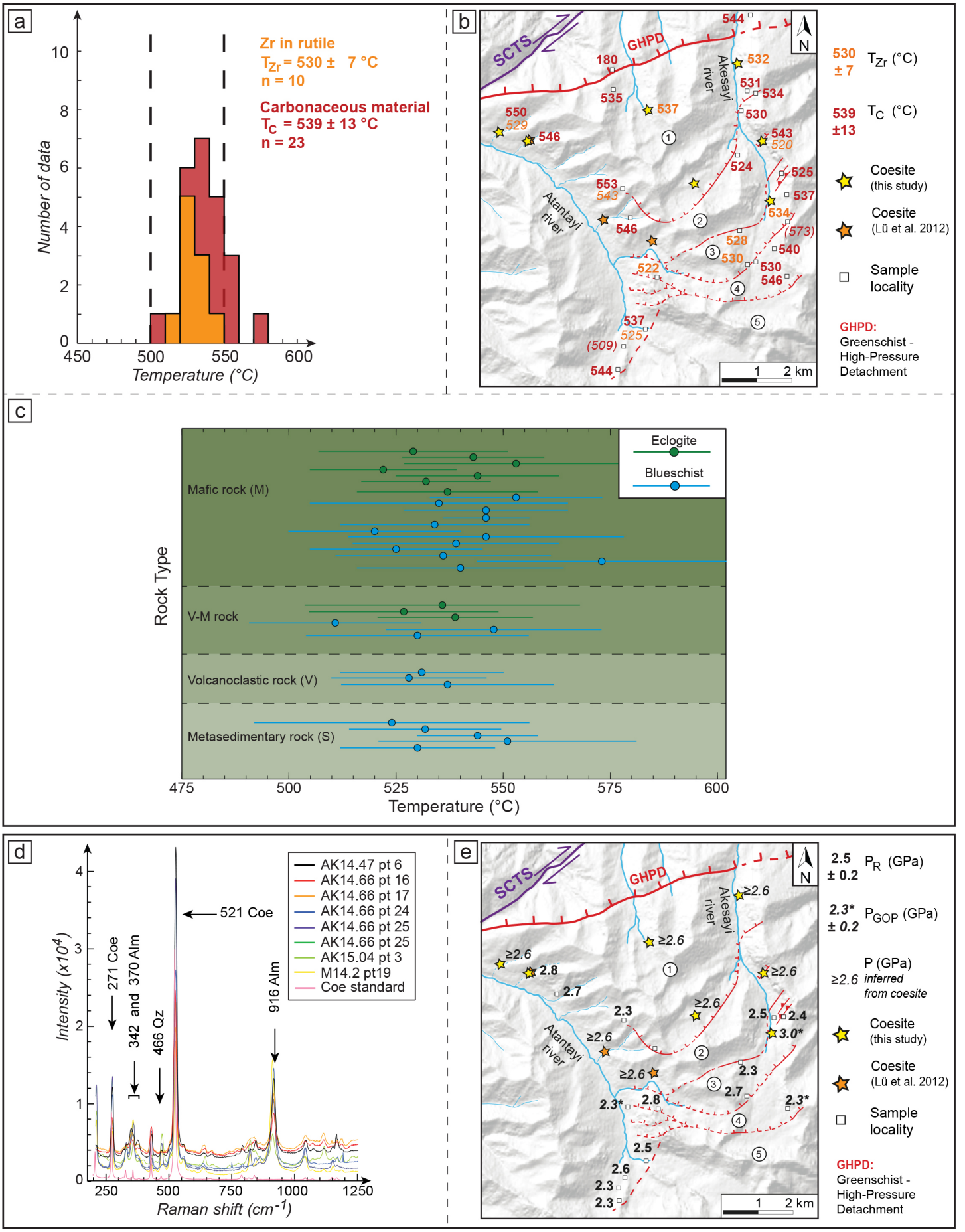
a
Zr in rutile
T_{Zr} = 530 ± 7 °C
n = 10
Carbonaceous material
T_C = 539 ± 13 °C
n = 23
Number of data
Temperature (°C)
b
SCTS
GHPD
Akesayi river
Atantayi river
544
180
532
535
537
531
534
550
529
530
546
543
520
524
525
553
543
537
534
546
(573)
528
540
530
522
530
546
537
525
(509)
544
1 2 km
N
530 ± 7 T_{Zr} (°C)
539 ±13 T_C (°C)
Coesite (this study)
Coesite (Lü et al. 2012)
Sample locality
GHPD: Greenschist - High-Pressure Detachment
c
Eclogite
Blueschist
Mafic rock (M)
V-M rock
Volcanoclastic rock (V)
Metasedimentary rock (S)
Rock Type
Temperature (°C)
d
AK14.47 pt 6
AK14.66 pt 16
AK14.66 pt 17
AK14.66 pt 24
AK14.66 pt 25
AK14.66 pt 25
AK15.04 pt 3
M14.2 pt19
Coe standard
521 Coe
271 Coe
342 and 370 Alm
466 Qz
916 Alm
Intensity (x10⁴)
Raman shift (cm⁻¹)
e
SCTS
GHPD
Akesayi river
Atantayi river
≥2.6
≥2.6
≥2.6
2.8
2.7
2.3
≥2.6
≥2.6
2.5
2.4
3.0*
≥2.6
2.3
≥2.6
2.7
2.3*
2.8
2.3*
2.5
2.6
2.3
2.3
1 2 km
N
2.5 ± 0.2 P_R (GPa)
2.3* ± 0.2 P_{GOP} (GPa)
P (GPa) inferred from coesite
Coesite (this study)
Coesite (Lü et al. 2012)
Sample locality
GHPD: Greenschist - High-Pressure Detachment

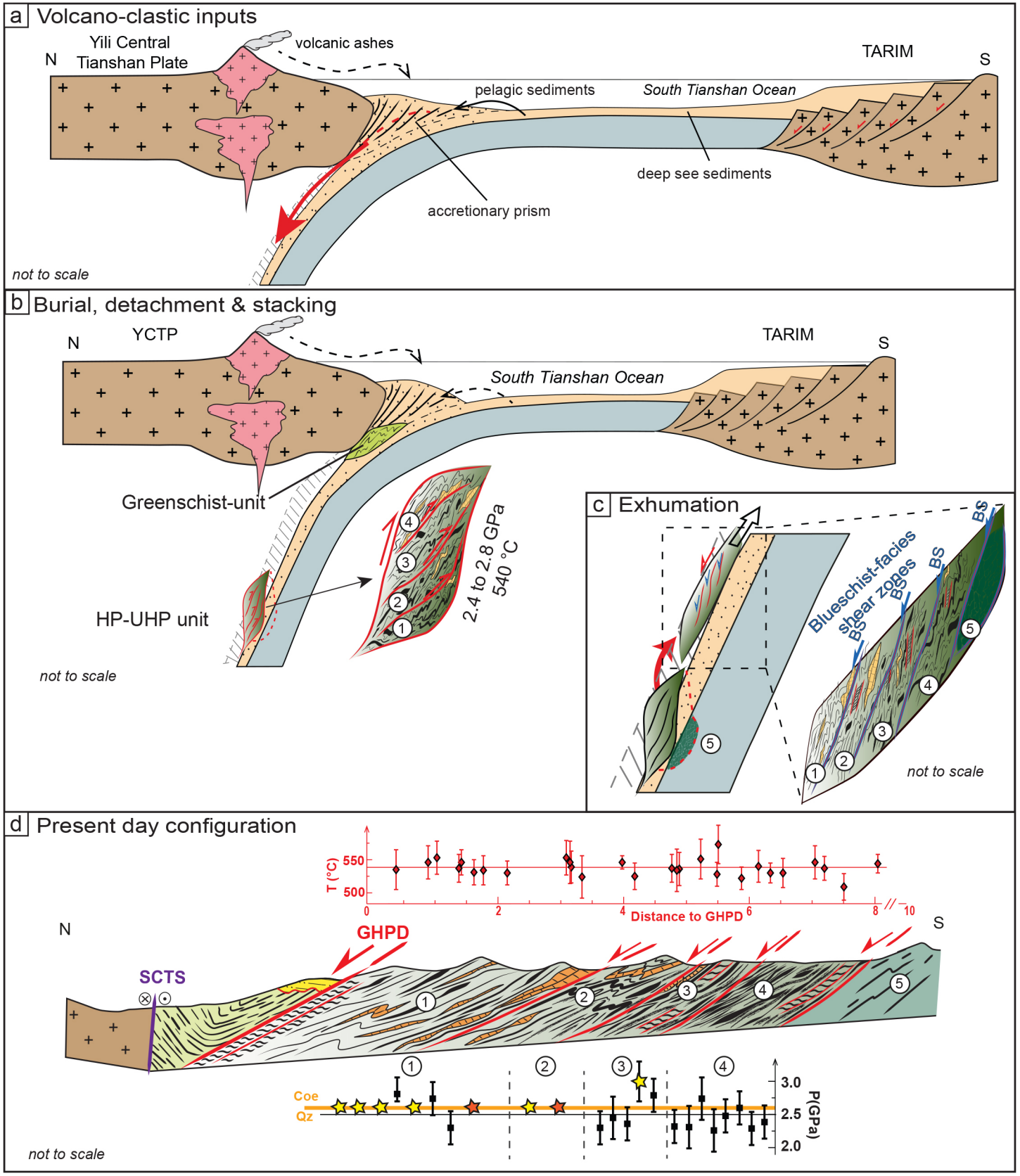
a Volcano-clastic inputs
N
Yili Central
Tianshan Plate
volcanic ashes
TARIM
S
pelagic sediments
South Tianshan Ocean
deep see sediments
accretionary prism
not to scale
b Burial, detachment & stacking
N
YCTP
TARIM
S
South Tianshan Ocean
Greenschist-unit
HP-UHP unit
2.4 to 2.8 GPa
540 °C
not to scale
c Exhumation
Blueschist-facies
shear zones
BS
not to scale
d Present day configuration
T (°C)
550
500
0
2
4
Distance to GHPD
6
8
10
N
S
GHPD
SCTS
Coe
Qz
3.0
2.5
2.0
P(GPa)
not to scale

Table 1: Deformation stages observed in the HP-UHP unit (see Fig. 6g)

	Deformation stage*				
	D_{n-1}	D_n	D_{n+1}	D_{n+2}	D_{n+3}
Associated deformation	Quartz inclusions and/or inclusion trails in garnets	Schistosity (S_n)	Crenulation schistosity (S_c) Folding	BS Shearing (C)	GS Shearing (C')
Minerals					
Chlorite					
Phengite					
Blue-Green Amphibole					
Blue Amphibole					
Epidote					
Garnet					
Omphacite					
Carbonate					
Scale**	mm-cm	mm-km	mm-hm	mm-km	cm-m
Metamorphic facies	BS-Ecl (?)	Ecl to BS	Ecl to BS	BS	BS-GS
Burial / exhumation	Burial	Burial to exhumation	Burial to exhumation	BS-facies exhumation	BS- to GS-facies exhumation

**: different deformation stages observed in the HP-UHP unit; **: observation scale for each deformation stage*

D: deformation; n+/-i: different stages; S_n: schistosity; S_c: crenulation schistosity; F: folding; C and C': shearing

Table 2: Representative major element composition of minerals of Tianshan metamorphic rocks

Sample	AK 14.19-1	AK 14.19-2	AK 14.33	AK 14.33	AK 14.62	AK 14.15	AK 14.19	AK 14.19	AK 15.0-	AK 15.0-	AK 14.0-	AK 14.3/	AK 14.33	FTS 2-7	AK 14.35-	AK 14.30	AK 14.66-	AK 14.35	AK 14.19-	AK 14.3	AK 14.3	K 14.19-	AK 14.20	FTS 2-7	FTS 2-7	M 14.8	M 14.8	AK 14.3	FTS 2-7	FTS 2-7	M 14.8	K 14.19-2	AK 14.33	FTS 2-7	AK 15.04
Type	*BS*	*BS*	*Ecl*	*Ecl*	*Ecl*	*Ecl*	*Ecl*	*Ecl*	*Ecl*	*Ecl*	*Ecl*	*Ecl*	*Ecl*	*Ecl*	*BS*	*BS*	*BS*	*BS*	*BS*	*Ecl*	*Ecl*	*Ecl*	*Ecl*	*Ecl*	*Ecl*	*GS*	*Ecl*	*Ecl*	*Ecl*	*GS*	*BS*	*Ecl*	*Ecl*	*Ecl*
Mineral	Gt rim	Gt core	Gt rim	Gt core	Gt rim	Gt rim	Gt mantle	Gt core	Cpx - incl	Cpx - ma	Cpx - ma	Cpx - ma	Cpx - incl	Cpx - incl	Phg	Phg	Phg	Pg	Bar	Gln	Gln	Gln	Gln	Bar	Fe-Gln	act	Ep - mat	Ep - mat	Ep - mat	Ep - inc	Chl	Chl	Ab	Cc	Ank
SiO_2	38.23	36.95	37.20	37.23	37.47	37.48	37.27	36.95	54.11	55.10	55.48	56.57	54.78	54.33	53.28	53.47	52.07	50.05	49.93	57.55	54.10	58.35	59.48	48.47	53.91	54.55	36.87	39.59	38.47	38.18	25.71	27.00	68.62	0.00	0.02
TiO_2	0.03	0.05	0.04	0.08	0.05	0.05	0.03	0.05	0.11	0.01	0.12	0.04	0.08	0.04	0.22	0.11	0.29	0.08	0.26	0.02	0.10	0.01	0.01	0.27	0.12	0.00	0.41	0.09	0.07	0.01	0.04	0.05	0.03	0.01	0.00
Al_2O_3	21.64	20.74	21.90	21.21	21.92	21.41	20.99	20.74	6.71	7.56	9.80	13.42	8.52	6.81	26.63	23.05	28.09	38.62	10.48	11.54	10.79	12.22	11.74	10.16	9.77	0.88	28.35	32.25	24.71	21.41	19.26	19.99	19.53	0.01	0.00
Cr_2O_3	n.d.	n.d.	n.d.	n.d.	n.d.	0.02	0.00	0.00	0.10	0.09	0.04	0.00	0.00	0.00	n.d.	0.00	0.00	n.d.	0.03			0.03	0.02	0.00	0.00	0.00	n.d.	n.d.	n.d.	n.d.	0.00	0.01	n.d.	0.00	11.01
FeO	28.85	34.60	26.61	29.71	27.51	30.11	34.84	34.60	12.42	11.06	6.69	4.79	9.84	16.98	2.50	2.75	2.50	0.46	13.49	10.64	13.23	9.30	8.87	19.07	15.61	9.25	0.00	0.00	0.00	0.00	18.89	22.56	0.13	0.11	0.05
Fe_2O_3	n.d.	n.d.	n.d.	n.d.	n.d.	n.d.	n.d.	n.d.	n.d.	n.d.	n.d.	n.d.	n.d.	n.d.	n.d.	n.d.	n.d.	n.d.	n.d.	0.00	0.00	n.d.	n.d.	n.d.	n.d.	n.d.	5.18	1.60	11.20	14.78	n.d.	n.d.	n.d.	n.d.	n.d.
MnO	0.21	2.48	0.73	1.72	0.24	0.45	1.08	2.48	0.04	0.04	0.02	0.00	0.15	0.08	0.00	0.04	0.03	0.02	0.10	0.02	0.09	0.00	0.08	0.08	0.03	0.11	0.07	0.00	0.01	0.27	0.16	0.08	0.04	0.04	0.09
MgO	3.39	2.18	2.00	1.58	4.51	3.08	2.43	2.18	6.16	6.10	7.33	6.05	6.46	3.51	3.49	4.32	2.92	0.13	11.36	9.36	9.02	10.21	10.55	7.98	8.35	17.38	0.04	0.02	0.11	0.02	19.60	17.76	0.00	0.01	14.48
CaO	8.03	2.63	11.36	8.09	7.79	6.99	3.65	2.63	13.56	12.62	13.11	10.16	12.21	8.35	0.00	0.02	0.03	0.09	7.42	0.31	2.44	0.44	0.53	5.70	2.32	13.14	24.73	24.72	23.44	23.31	0.15	0.01	0.15	54.23	27.80
Na_2O	0.02	0.08	0.03	0.00	0.00	0.04	0.02	0.08	6.55	7.07	7.32	8.76	7.43	9.06	0.51	0.13	0.58	6.89	3.66	6.69	5.97	6.91	7.33	4.81	6.46	0.19	0.01	0.07	0.00	0.00	0.00	0.01	11.27	0.00	0.04
K_2O	0.00	0.01	0.01	0.01	0.01	0.02	0.02	0.01	0.00	0.00	0.01	0.00	0.00	0.01	9.93	10.35	9.66	0.56	0.24	0.02	0.09	0.03	0.02	0.31	0.11	0.03	0.00	0.00	0.00	0.00	0.01	0.01	0.02	0.00	0.00
Total	*100.40*	*99.68*	*99.88*	*99.63*	*99.50*	*99.65*	*100.32*	*99.68*	*99.75*	*99.63*	*99.92*	*99.78*	*99.47*	*99.16*	*96.55*	*94.25*	*96.17*	*96.90*	*96.97*	*96.14*	*95.82*	*97.52*	*98.63*	*96.86*	*96.66*	*95.52*	*95.66*	*98.33*	*98.01*	*97.97*	*83.82*	*87.48*	*99.78*	*54.40*	*53.49*
Si	6.01	5.99	5.90	5.98	5.92	5.97	5.98	5.99	1.99	2.01	1.98	2.00	1.99	0.00	3.49	3.60	3.42	3.12	7.15	7.96	7.69	7.92	8.01	7.11	7.70	7.91	2.92	3.01	3.03	3.06	2.75	2.80	3.00		
Ti	0.00	0.01	0.01	0.01	0.01	0.01	0.00	0.01	0.00	0.00	0.00	0.00	0.00	0.31	0.01	0.01	0.01	0.00	0.03	0.00	0.01	0.00	0.00	0.03	0.01	0.00	0.02	0.01	0.00	0.00	0.00	0.00	0.00		
Al	4.01	3.96	4.10	4.02	4.01	4.02	3.97	3.96	0.29	0.33	0.41	0.56	0.36	0.00	2.05	1.83	2.17	2.84	1.77	1.88	1.81	1.96	1.86	1.76	1.64	0.15	2.65	2.88	2.29	2.02	2.43	2.45	1.01		
Cr	0.00	0.00	0.00	0.00	0.00	0.00	0.00	0.00	0.00	0.00	0.00	0.00	0.00	0.54	n.c.	n.c.	0.00	n.c.	0.00	0.00	0.00	0.00	0.00	0.00	0.00	0.00	0.00	0.00	0.00	0.00	n.c.	n.c.	0.00		
Fe_{tot}	3.79	4.69	3.53	3.99	3.63	4.01	4.68	4.69	0.38	0.34	0.20	0.14	0.30	0.20	0.14	0.16	0.14	0.02	1.62	0.31	0.39	1.06	1.00	2.34	1.86	1.12	0.34	0.09	0.66	0.89	1.69	1.96	0.01		
Fe^{2+}	3.79	4.69	3.53	3.99	3.62	4.01	4.68	4.69	0.19	0.19	0.12	0.05	0.18	0.00	n.c.	n.c.	n.c.	n.c.	1.08	0.92	1.18	0.81	0.96	1.61	1.45	1.12	n.c.	n.c.	n.c.	n.c.	1.69	1.96	0.01		
Fe^{3+}	0.00	0.00	0.00	0.01	0.01	0.00	0.00	0.00	0.19	0.15	0.08	0.10	0.12	0.20	n.c.	n.c.	n.c.	n.c.	0.54	1.23	1.57	0.25	0.04	0.73	0.41	0.00	0.34	0.09	0.66	0.89	n.c.	n.c.	n.c.		
Mn	0.03	0.34	0.10	0.24	0.03	0.06	0.15	0.34	0.00	0.00	0.00	0.00	0.01	0.34	0.00	0.00	0.00	0.00	0.01	0.00	0.01	0.00	0.01	0.01	0.00	0.01	0.00	0.00	0.00	0.02	0.02	0.01	0.00		
Mg	0.79	0.53	0.47	0.38	1.06	0.73	0.58	0.53	0.34	0.33	0.39	0.32	0.35	0.67	0.34	0.43	0.29	0.01	2.42	1.93	1.91	2.07	2.12	1.75	1.78	3.76	0.00	0.00	0.01	0.00	3.13	2.75	0.00		
Ca	1.35	0.46	1.93	1.39	1.32	1.19	0.63	0.46	0.53	0.49	0.50	0.38	0.47	0.00	0.00	0.00	0.00	0.01	1.14	0.05	0.37	0.06	0.08	0.90	0.36	2.04	2.10	2.01	1.98	2.00	0.02	0.00	0.01		
Na	0.01	0.03	0.01	0.00	0.00	0.01	0.01	0.03	0.47	0.50	0.51	0.60	0.52	0.27	0.06	0.02	0.07	0.83	1.02	1.79	1.65	1.82	1.91	1.37	1.79	0.05	0.00	0.01	0.00	0.00	0.00	0.00	0.96		
K	0.00	0.00	0.00	0.00	0.00	0.00	0.00	0.00	0.00	0.00	0.00	0.00	0.00	0.00	0.83	0.89	0.81	0.05	0.04	0.00	0.02	0.01	0.00	0.06	0.02	0.01	0.00	0.00	0.00	0.00	0.00	0.00	0.00		
XMg	0.17	0.10	0.12	0.09	0.23	0.15	0.11	0.10	0.47	0.49	0.66	0.69	0.54	0.77	0.71	0.74	0.35	n.c.	0.69	0.68	0.62	0.72	0.69	0.52	0.55	0.77	n.c.	n.c.	n.c.	n.c.	0.65	0.58	n.c.		
Alm	63.56	77.97	58.51	66.52	60.05																														
Pyr	13.30	8.77	7.85	6.33	17.57																														
Grs	22.67	7.60	31.99	23.12	31.66																														
Sps	0.48	5.66	1.63	3.91	0.64																														
And	0.00	0.00	0.02	0.12	0.18																														
Di									0.34	0.33	0.40	0.30	0.35	75.00																					
Hd									0.19	0.18	0.08	0.09	0.12	0.17																					
Jd									0.26	0.34	0.38	0.56	0.34	0.17																					
Acm									0.19	0.16	0.12	0.05	0.18	0.31																					
K/Na+K															0.93	0.93	0.93	0.05																	
(Ca+Na) (B)																			2.00	1.84	2.00	1.88	2.00	2.00	2.00	2.04									
Na (B)																			0.86	1.79	1.63	1.82	1.10	1.10	1.65	0.00									
(Na+K) (A)																			0.20	0.00	0.03	0.01	0.32	0.32	0.17	0.06									
$Fe^{3+}/(Fe^{3+}+Al^{VI})$																			0.37	0.15	0.21	0.12	0.46	0.46	0.24	0.00									
Pistachite (Fe)																											0.11	0.03	0.22	0.31					
Zoïsite (Al)																											0.89	0.97	0.78	0.69					

X_{Mg}=Mg/(Fe_{2+}/Mg); Alm: almandine, Grs: grossular, Prp: pyrope, Sps: spessartine, And: andradite, Di: diopside, Hd: hedenbergite, Jd: jadeite, Acm: acmite. Fe3+ was calculated assuming stoichiometric mineral compositions

n.d.: not determined, n.c.: not calculated

Minerals structural formulae calculation are based on a number of oxygens of : 12 for garnet, 8 for clinopyroxenes, 11 for phengite, for 12.5 epidote, and 6 for albite

Amphibole structural formulae are based on 23 oxygens with Fe2+/Fe3+ estimation assuming ∑13 cations - except for Fe-Mg-Mn amphiboles where ∑15 is applied.